Doctoral Dissertations and Master's Theses

Fall 12-2017

Implementation and Verification of a Synthetic Eddy Method (SEM) in the Eagle3d Compressible Flow Solver

Patrick Kopper
Embry-Riddle Aeronautical University

IMPLEMENTATION AND VERIFICATION OF A SYNTHETIC EDDY

METHOD (SEM) IN THE EAGLE3D COMPRESSIBLE FLOW SOLVER

A Thesis

Submitted to the Faculty

of

Embry-Riddle Aeronautical University

by

Patrick Kopper

In Partial Fulfillment of the

Requirements for the Degree

of

Master of Science in Aerospace Engineering

December 2017

Embry-Riddle Aeronautical University
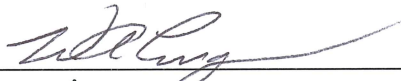
Daytona Beach, Florida

IMPLEMENTATION AND VERIFICATION OF A SYNTHETIC EDDY METHOD (SEM) IN THE EAGLE3D COMPRESSIBLE FLOW SOLVER
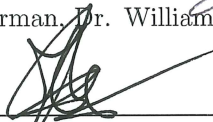
by

Patrick Kopper

A Thesis prepared under the direction of the candidate's committee chairman, Dr. William Engblom, Department of Aerospace Engineering, and has been approved by the members of the thesis committee. It was submitted to the School of Graduate Studies and Research and was accepted in partial fulfillment of the requirements for the degree of Master of Science in Aerospace Engineering.

THESIS COMMITTEE
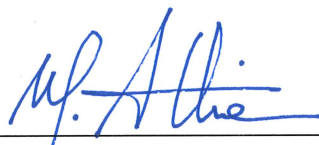
_____
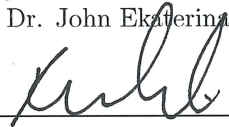Chairman, Dr. William Engblom

_____
Member, Dr. John Ekaterinaris

_____
Member, Dr. Reda Mankbadi

_____   11.29.2017
Graduate Program Coordinator, Dr. Magdy Attia   Date

_____   11/29/2017
Dean of College of Engineering, Dr. Maj Mirmirani   Date

_____   12/1/17
Vice Chancellor, Academic Support, Dr. Christopher Grant   Date

ACKNOWLEDGMENTS

I would like to thank my friends and family for their unwavering support, love, care and belief. They encouraged me to follow my path when I had doubts and made me the person I am today. I could always rely on their honest advice and they motivated me to bring out the best of me. They continue to be my source of inspiration and encouragement.

I would like to thank my thesis supervisor, Dr. William Engblom, for being my mentor in academic matters and beyond. He motivated me from the minute I met him and guided me ever since. He has always been available to provide his support and even sacrificed parts of his own work and enjoyment to ensure he would address all my concerns completely. The talks and discussions with him were characterized by kindness and patience and he would always consider my opinion on a topic. His determination and striving for excellence, even when doubted by others, continues to impress me and only his hard work made this thesis possible.

I would like to thank Dr. John Ekaterinaris for his valuable feedback and council. His immense knowledge continued to impress me and provided points of view otherwise inaccessible. I would like to extend my thankfulness to Dr. Reda Mankbadi, whose experience and advise put things into perspective and kept my mind open.

TABLE OF CONTENTS

LIST OF TABLES

LIST OF FIGURES

SYMBOLS

a_{ij}	Lund coefficient
c_p	isobaric specific heat capacity
e	specific internal energy
$\mathbf{f_V}$	body force
$\mathbf{g}$	gravitational force
k	turbulent kinetic energy
p	static pressure
$\mathbf{q}$	heat flux
$q_{+/i}$	left/right Roe state
$\hat{q}$	average value at cell boundary
m	mass
n	polynomial degree
$\mathbf{n}$	normal vector
u'	streamwise velocity perturbation
$\mathbf{u}$	velocity vector
u_τ	friction velocity
v'	transverse velocity perturbation
w'	spanwise velocity perturbation
t	time
C_{f_b}	skin friction coeffiction (bulk velocity)
C_{f_f}	skin friction coeffiction (free-stream velocity)
C_s	Smagorinsky coefficient
F^{conv}	convective flux
F^{HLLC}	HLLC flux
$\mathbf{I}$	identity matrix
N	number of eddies/polynomial degree
Re_θ	momentum thickness Reynolds number
Re_τ	friction Reynolds number
$S_{n,k}$	smoothness indicator
T	static temperature
T_0	total temperature
U_{bulk}	bulk velocity
U_{wall}	wall velocity
U_∞	free-stream velocity
V_B	box volume
V_{cell}	cell volume

α	thermal conductivity
δ	boundary layer thickness/channel half width
ϵ	turbulent dissipation
$\epsilon_{\beta jl}$	Levi-Civita symbol
λ_j	WENO coefficient
γ_j	linear weight
ν	kinematic viscosity
ρ	density
σ	eddy length scale
τ	viscous stress tensor
τ_w	wall shear stress
Δ_{Cell}	local cell size
Ω	control volume

ABBREVIATIONS

BCD   Bounced Central-Differencing
BSL   Wilcox-Stress-Baseline
CFD   Computational Fluid Dynamics
DNS   Direct Numerical Simulation
DFSEM   Divergence-free Synthetic Eddy Method
ELES   Embedded Large Eddy Simulation
ERAU   Embry-Riddle Aeronautical University
FFT   Fast Fourier Transform
HLLC   Harten, Lax and van Leer with contact restoration
LES   Large Eddy Simulation
NASA   National Aeronautics and Space Administration
RANS   Reynolds-Averaged Navier-Stokes
RST   Reynolds Stress Tensor
SEM   Synthetic Eddy Method
SST   Shear-Stress-Transport
UDF   User Defined Function
WENO   Weighted Essentially Non-Oscillatory Reconstruction
ZLES   Zonal Large Eddy Simulation

ABSTRACT

Kopper, Patrick MSc, Embry-Riddle Aeronautical University, December 2017. Implementation and Verification of a Synthetic Eddy Method (SEM) in the Eagle3D Compressible Flow Solver.

The objective of this thesis is to implement and evaluate a Synthetic Eddy Method (SEM) into the Eagle3D compressible flow solver. Both the ability of Eagle3D to resolve unsteady turbulent flow field and capability of the SEM to reproduce given Reynolds stress profiles to start realistic turbulent behavior are verified using common academic cases. Eagle3D is a Computional Fluid Dynamics (CFD) solver using a novel combination of a Bounded Central Differencing (BCD) scheme with Weighted Essentially Non-Oscillatory (WENO) approximation to reduce numerical dissipation. SEM is a modern synthetic turbulence method able to reproduce an arbitrary Reynolds stresses specification on discretionary geometries while keeping computational costs low. The Large-Eddy Simulation (LES) capability of Eagle3D is evaluated using the flow over a cylinder and compared to results by ANSYS Fluent. The SEM is used to reproduce unsteady inlet conditions for channel and flat plate cases and relayed into Eagle3D. Common flow parameters such as skin friction, Reynolds stresses and velocity components are compared against analytic, Direct Numerical Simulation (DNS)

and periodic LES to estimate the performance of this solver combination in accuracy and development length. Parametric studies of grid dependence, varying upstream Reynolds-Averaged Navier-Stokes (RANS) data and prescribed eddy length scale are performed. Modifications to the SEM are prescribed and tested where suitable. Further studies and modifications to the SEM based on the obtained data are suggested.

1. Introduction

The application of eddy resolving methods in Computational Fluid Dynamics (CFD) for research and development of propulsive flow paths is of considerable interest in the aerospace community. Although the aerospace industry largely depends on the Reynolds-Averaged Navier-Stokes (RANS) equations, eddy resolving methods offer the potential of higher fidelity treatment of the turbulence effects crucial in propulsive flows. Unfortunately, eddy resolving methods, like Large-Eddy Simulation (LES), often pose excessive computational cost. Accurate simulation of propulsion systems also often involve a wide range of flow regimes from very low subsonic (e.g., film cooling of turbine blades) to highly compressible (e.g., transonic flow over turbine blades), which further complicates the use and cost effectiveness of eddy resolving methods.

It has been shown in numerous publications during the last quarter century, that LES results show a large dependence on the accurate reproduction of the time-accurate inflow turbulent fluctuations (Druault et al., 2005; Rynell, Efraimsson, Chevalier, & Abom, 2016; Wu, 2017). Various methods for modeling of time-varying inflow turbulence have been suggested over the last decades which depend on available steady-state (e.g., RANS generated) data. The focus of the current effort focuses on the Synthetic Eddy Method (SEM) as first proposed by Jarrin et al. (Jarrin, Ben-

hamadouche, Laurence, & Prosser, 2006) due to the main advantage of being able to reproduce an arbitrary Reynolds Stress distribution over an inflow plane while keeping computational requirements low, with typically under 5% of total calculation time. Despite these promising prospects on the suitability of the SEM for a wide range of applications (e.g., film cooling of turbine blades), implementations in commonly used codes is rare with incomplete or deficient realization in Code_Saturne and OpenFOAM and completely unavailable in commercial codes such as ANSYS Fluent.

The Eagle3D flow solver has been under development at ERAU with the long-term goal of offering a practical, high-fidelity tool for entire propulsive flowpaths (from "tip-to-tail"), including eddy resolving techniques. Originally developed as a general purpose, chemically-reacting, RANS-based, structured, density-based finite-volume flow solver (Engblom, Fletcher, & Georgiadis, 2007), this code is well validated for steady-state, high-speed propulsive flows. During the course of this recent development effort, which included collaboration with NASA Glenn Research Center, the code was modified to offer high-fidelity treatment of the unsteady, low-speed subsonic flows commonly examined in development of eddy-resolving techniques. More specifically, a novel Bounded Central Differencing (BCD) flux scheme, to be described later, was implemented to ensure stability and low-dissipation results. This development was completed to prepare the code to be effective for the present effort.

The primary purpose of the current effort is to implement the Jarrin style SEM capability into Eagle3D and evaluate and verify the SEM capability in combination with Eagle3D's BCD scheme. A related early goal was to verify that the aforementioned

BCD implementation in Eagle3D appropriately resolves the unsteady turbulent eddy field for the canonical case of 3-D flow over a cylinder (relative to ANSYS Fluent). The SEM implementation, in combination with Eagle3D, is then evaluated using two commonly used 3-D cases in the literature, the channel and the flat plate. The sensitivity of results to various SEM model parameters and eddy-resolving settings is evaluated. It is important to mention that no related literature has been published on the accuracy of a BCD flux scheme within a density-based LES code, in combination with a SEM for unsteady inflow turbulence.

2. Methodology

This chapter gives an introduction to the computational methods used in this thesis. It includes background and discussion of both the flow solver and synthetic turbulence method utilized herein. All quantities in bold denote vector quantities.

2.1 Eagle3D Flow Solver

Eagle3D is a finite-volume, density-based, cell-centered flow solver. It solves the Navier-Stokes equations in the integral form listed below, including the continuity equation

$$\frac{\partial}{\partial t} \int_\Omega \rho dV = - \int_{\delta\Omega} \rho \mathbf{u} \cdot \mathbf{n}\, dS \tag{2.1}$$

the momentum equation (with body forces acting on the volume summarized as $\mathbf{f}_V$)

$$\frac{\partial}{\partial t} \int_\Omega \rho \mathbf{u}\, dV + \int_{\partial\Omega} (\rho \mathbf{u}\mathbf{u}) \cdot \mathbf{n}\, dS = \int_{\partial\Omega} \boldsymbol{\sigma} \cdot \mathbf{n}\, dS + \int_\Omega \rho \mathbf{f}_V\, dV \tag{2.2}$$

where $\sigma = \tau - p\mathbf{I}$ denotes the viscous stress tensor including pressure terms and the energy equation

$$\begin{aligned}
\frac{\partial}{\partial t} \int_\Omega \rho \left(e + \frac{1}{2}|\mathbf{u}|^2 \right) dV = & -\int_{\partial\Omega} \rho \left(e + \frac{1}{2}|\mathbf{u}|^2 \right) \mathbf{u} \cdot \mathbf{n} dS - \int_{\partial\Omega} p\mathbf{u} \cdot \mathbf{n} dS \\
& + \int_{\partial\Omega} (\boldsymbol{\tau}\mathbf{u}) \cdot \mathbf{n} dS + \int_\Omega \rho \mathbf{g} \cdot \mathbf{u} dV \\
& + \int_{\partial\Omega} \rho \mathbf{q} \cdot \mathbf{n} dS + \int_{\partial\Omega} \alpha \nabla T \cdot \mathbf{n} dS
\end{aligned} \tag{2.3}$$

where **g** denotes gravitational force, τ the viscous stress tensor and **q** the sum of all heat fluxes (Anderson, 1995; Ferziger, 2008).

2.1.1   Pressure-based and Density-based Solvers

In general, the Navier-Stokes equations form a coupled system of equations. However, especially for low-speed flows, the coupling of the continuity and momentum equations with the energy equation becomes weak and completely decoupled for incompressible flow. As many applications deal with relatively low Mach number flows, pressure-based solvers have evolved as a type of flow solvers that solves the continuity and momentum equations separately from the energy equation and later connects this equation through an outer loop iteration. These solvers can further be split into a segregated (e.g., SIMPLE or PISO) approach which connects the continuity and momentum equation through a Poisson equation in an inner loop and a coupled approach which solves both equations as a system. As the system of equations to solve for one time step is smaller for pressure-based solvers, they tend to be generally faster per iteration and the dominant choice for subsonic flows. For trans- and supersonic flows, the mentioned decoupling poses challenges to these solvers (ANSYS, Inc., 2010).

In contrast, density-based solvers tend to be the solvers of choice for highly compressible flows. These solvers are typically slower per iteration as they solve the entire system of equations simultaneously, but do not struggle from compressible effects. However, in low-speed flows, the small convective velocity compared to the acoustic speed leads to the equations becoming increasingly stiff (Roller & Munz,
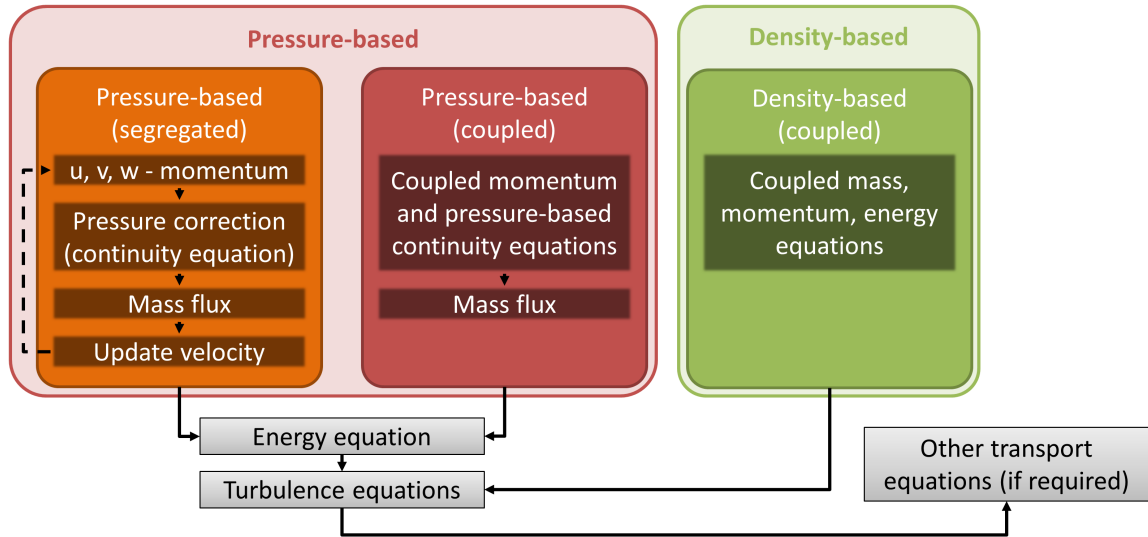
Figure 2.1 Schematics of pressure- and density-based solvers (with material from Ansys Inc. (ANSYS, Inc., 2010))

2000). Historically, density-based solvers used high-dissipation upwind schemes to compensate for the increasing stiffness of the Navier-Stokes equations when applied to low-speed flows. However, this approach leads to sub-accurate results especially when combined with Large-Eddy Simulations (LES, see sec. 2.2).

2.1.2 Eagle3D Bounded Central Differencing (BCD) scheme

Winkler et al. recently introduced a bounded central differencing approach to use higher order central differencing schemes and their inherently low dissipation without sacrificing stability (Winkler, Dorgan, & Mani, 2012). Winkler et al. followed the

approach by Tajallipour et al. (Tajallipour, Owlam, & Paraschivoiu, 2009) to use Roe's method and define the convective flux as

$$
\begin{aligned}
\mathbf{F}^{conv} \cdot \mathbf{n}_{ij} = & \frac{1}{2}(1 - \gamma)\left(\mathbf{F}^{conv}(q_+) + \mathbf{F}^{conv}(q_-)\right) \cdot \mathbf{n}_{ij} \\
& - \gamma \left[\frac{1}{2}\left|\hat{A}(\hat{q}, \mathbf{n}_{ij}\right|(q_+ - q_-)\right]
\end{aligned}
\tag{2.4}
$$

where q_+ and q_- represent the left and right Roe states and $\hat{q}$ is the average value at the boundary of the cell. The parameter γ then acts as a blending between full central difference scheme for $\gamma = 0$ and the original scheme for $\gamma = 1$. Tajallipour et al. proposed to set the value of γ depending on the presence of a wiggle which is assumed to be present if any variable ϕ fulfills

$$
(\phi_i - \phi_{i-1})(\phi_{i+1} - \phi_i) < 0
\tag{2.5}
$$

$$
(\phi_{i+2} - \phi_{i+1})(\phi_{i+1} - \phi_i) < 0
\tag{2.6}
$$

Eagle3D builds on the work by Winkler et al. to define γ as a blending parameter. To achieve the required low-dissipation for LES, Eagle3D attempts to improve on the accuracy of Winkler et al. by combining the central differencing scheme with a fifth-order Weighted Essentially Non-Oscillatory Reconstruction (WENO) scheme.

WENO defines a stencil of required order and takes the weighted average of the polynomials from the whole stencil as

$$
q_i^{WENO}(x) = \sum_{j=0}^{n} \lambda_j p_{n,j}(x)
\tag{2.7}
$$

with the adaptive weighting obtained via a oscillations (or smoothness) indicator defined as defined by Jiang et al. (Jiang & Shu, 1996) as

$$
S_{n,k} = S(p_{N,k}) = \sum_{i=1}^{n} \int_{q_i} |q_i|^{i-1} \left(\frac{\partial^i}{\partial x^i} p_{n,k}(x)\right)^2 dx
\tag{2.8}
$$

where n is the desired polynomial degree. Defining γ_j with $\sum_{i=j}^{N} \gamma_j = 1$ as the linear weights obtained from literature, this gives

$$\lambda_j = \frac{\tilde{\lambda}_j}{\sum_{j=1}^{N} \tilde{\lambda}_j} \qquad \text{with} \qquad \tilde{\lambda}_j = \frac{\gamma_j}{(\epsilon + S_{n,k})^2} \tag{2.9}$$

Eagle3D uses a 5th order WENO to estimate the upwind-biased states q_i for the Riemann problem at the cell faces. Eqn. (2.4) is modified to combine a Harten, Lax and van Leer with contact restoration (HLLC) solver (Toro, Spruce, & Speares, 1994) with a 2nd order central differencing scheme, both using the cell face values provided by WENO. The resulting formulation for the inviscid fluxes is then

$$\begin{aligned}
\mathbf{F}^{conv} \cdot \mathbf{n}_{ij} =& \frac{1}{2}(1 - \gamma)\left(\mathbf{F}^{conv}(q_+) + \mathbf{F}^{conv}(q_-)\right) \cdot \mathbf{n}_{ij} \\
& + \gamma\left[\mathbf{F}^{HLLC}(q_+, q_-)\right]
\end{aligned} \tag{2.10}$$

The value of γ in Eagle3D is restricted to the empirical range $\gamma \in [0.8; 0.99]$. Eagle3D adaptively adjusts the value of γ using eqn. (2.5) and (2.6) with the change per time step restricted to 0.0025. As the formulation of the 2nd order central differencing scheme using the WENO approximations on the cell faces is rather unique, a classical cell-center based 4th order central differencing scheme is also available at the user's discretion.

The viscous fluxes in Eagle3D are modeled using a combination of the thin-layer gradient contribution plus the cross-derivative gradient contribution, as convention-ally done in structured grid solvers. Eagle3D applies cell-based implicit Gauss-Seidel time advancement scheem with 2nd order accurate temporal resolution.

2.2   Large Eddy Simulation

Turbulence is compromised of random motion over a wide range of scales with the large scales containing most of the energy and energy transfer mainly happening from larger to smaller scales through the energy cascade. Given sufficient temporal and spectral resolution, these turbulent scales can be completely described by the Navier-Stokes equations in Direct Numerical Simulation (DNS) down to the Kolmogoroff microscales where the energy is dissipated through viscous effects (see fig. 2.2).
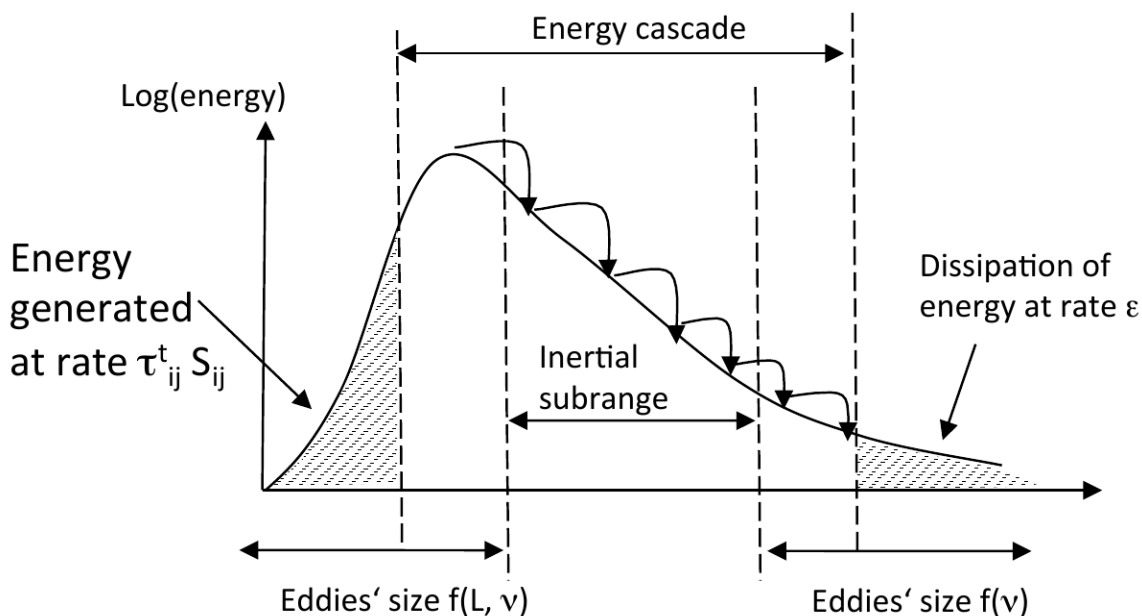
Figure 2.2 Representation of the turbulent energy cascade (Lamanna et al., 2015)

However, for all practical applications the requirements on memory and computational power of DNS remain too high to be usable which gave rise to Large-Eddy simulations (LES). LES utilizes the fact that the large scales are the carry most of the turbulent energy and therefore have the most influence on the mean flow. LES only

resolves eddies down to a certain length scale with the velocity field either explicitly filtered by convolution

$$\bar{u}_i = G_{\Delta_{Cell}} * u_i \tag{2.11}$$

where the convolution kernel $G_{\Delta_{Cell}}$ is used to eliminate scales smaller than Δ_{Cell} (Subgrid Scales (SGS), see Pope et al. (Pope, 2015) for a complete description) or implicitly filtered due to the spatial resolution of the grid. The former method, the explicit LES, usually relies on a subgrid model to simulate the effect of the filtered eddies, the Smagorinsky model being the most well known. The latter method, the implicit LES, leaves the dissipation of the underresolved kinetic energy purely to the numerical dissipation of the used scheme (Meneveau, 2010).

2.2.1   Smagorinsky-Lilly model

In general, for explicit LES the effect of the unresolved eddy scales are modeled with a Boussinesq approach, estimating the momentum flux to be proportional to the rate of strain of the resolved scales. Unlike a RANS approach, where this approach only relates to the mean flow, a subgrid model takes unsteady turbulent scales into account. The most commonly used subgrid scale (SGS) model follows the approach by Smagorinsky (Smagorinsky, 1963), who modeled the eddy-viscosity as

$$\tau_{ij} - \frac{1}{3}\tau_{kk}\delta_{ij} = -2(C_s\Delta)|\bar{S}|S_{ij} \tag{2.12}$$

From this, the eddy-viscosity of the unresolved scales is estimated by

$$\nu_{SGS} = (C_s\Delta)|\bar{S}| \tag{2.13}$$

with $\bar{S}$ defined as

$$\bar{S} = \sqrt{2S_{ij}S_{ij}} \tag{2.14}$$

and Δ being the local cell dimension (Meneveau, 2010). The coefficient C_s was found by Lilly to be $C_s \approx 0.16$ (modern agreement is $Cs = 0.1 - 0.2$) which coined the term Smagorinsky-Lilly model (Lilly, 1967). Effective local viscosity is then calculated as the sum of laminar and eddy-viscosity as

$$\nu_{eff} = \nu_{lam} + \nu_{SGS} \tag{2.15}$$

2.2.2 Zonal RANS-LES simulation

Even with recent improvements in computing power, LES of complete aircraft remains too computationally expensive to be practicable for industrial applications. Zonal Large Eddy Simulation (ZLES, sometimes also called Embedded Large Eddy Simulation [ELES]) is not a model per se, but a collective term for simulations restricting the LES to the immediate area of interest and covering other areas with Reynolds-averaged Navier-Stokes (RANS) simulations or a comparable method. Depending on the extent of said area of interest compared to the overall simulation volume, ZLES allows for a signification reduction in computing power requirements of or exceeding 50 % of total computational time (Zhang, Schröder, & Meinke, 2010; Geurts, Meinke, & Schröder, 2013).
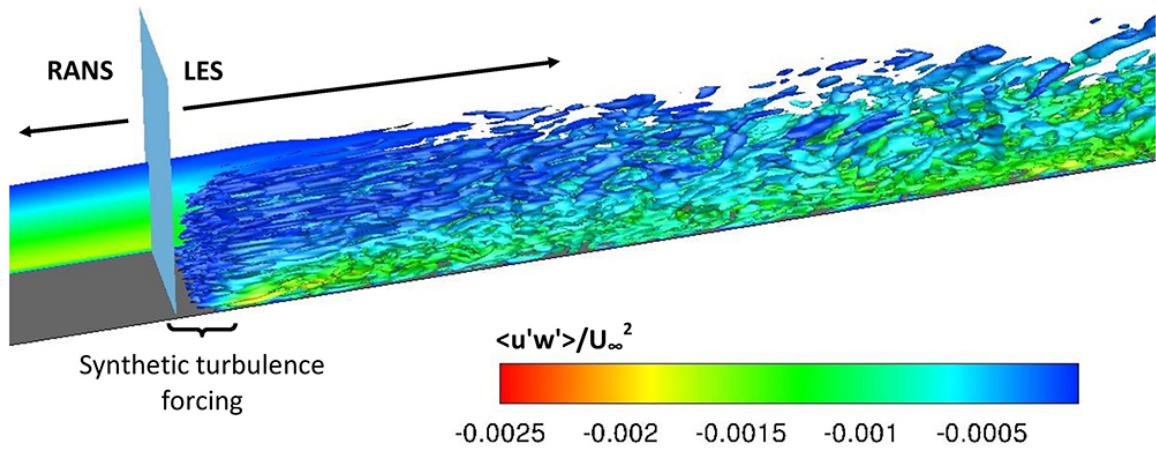
Figure 2.3 Illustration of ZLES coupling via Synthetic turbulence forcing (Francois, 2015)

While ZLES can reduce the overall computing power, it requires special treatment at the zone boundary to ensure consistent behavior. Usually, a synthetic turbulence method is chosen to reconstruct unsteady flow quantities from available steady-state results. These methods come at an additional computational cost and with individual weaknesses, so a careful balance must be found between a minimization of the LES zone computational cost and the accuracy of the turbulent flow data reconstruction. The following section 2.3, and especially subsection 2.3.2, aims to give a quick but comprehensive overview of the most commonly used turbulence generation methods.

2.3   Turbulence Generation Methods

Turbulence generation method in the context of this thesis refers to any computational method generating unsteady data deemed suitable as an inflow condition for a LES without having the actual time-dependent data to rely on. Special emphasis

is put on the accuracy of each method, its computational cost and suitability to work for an arbitrary upstream flow field.

2.3.1 Recycling Methods

Recycling methods differ from other methods of turbulence inlet generation since they do not employ a specialized set of equations. Recycling relies solely on the Navier-Stokes equations themselves. For fully developed turbulence, the mean flow quantities remain constant, independent of the downstream distance. Recycling methods utilize this fact by running a precursor simulation with periodic boundary conditions at the inlet and outlet, therefore "recycling" its own inlet data. After turbulent behavior is initially started by introducing arbitrarily shaped disturbances, a recycling method is run on its own and the inflow data of the actual simulation is extracted once realistic turbulence has been sustained. While recycling methods provide the most accurate turbulent inflow data, their key limitations are their high demand on computing power and their restriction to fully developed flows (Jarrin, 2008). A modification using a rescaling/recycling approach by separating the flow into mean and fluctuation parts and scaling them according to the similarity laws of the corresponding flow region has been shown by Lund et al. (Lund, Wu, & Squires, 1998), but is still limited to equilibrium boundary layers (Jarrin, 2008).

2.3.2   Synthetic Turbulence Methods

The following section focuses on approximate methods to generate a suitable inflow field for LES. It is assumed that mean statistical data at the inflow place is available, either from upstream RANS simulations or experimental data. As these methods inevitably contain some error, they generally require a certain "development section" to be added to the simulation. As more accurate synthetic turbulence methods generally come with higher computational cost, usually a trade-off has to be made between minimizing the extent of the development section and reducing the cost of the generation method (Lund et al., 1998).

Random Fluctuations

The simplest method of simulating turbulent inflow data is describing the instantaneous velocity as the sum of the mean velocity profile plus some random disturbances. One-point, second-order statistics such as the Reynolds stress tensor can be matched by an appropriate scaling of the random amplitudes (Lund et al., 1998). However, the generated data lacks spatial and temporal coherence and the energy is spread across all wave numbers. As such, the turbulence either dies out completely (Jarrin et al., 2006) or takes a long development length to transform into realistic turbulent behavior (Lund et al., 1998). Moreover, Klein et al. were able to prove that the downstream behavior of the random fluctuations method is similar to imposing a laminar profile at the inlet (Klein, Sadiki, & Janicka, 2003).

Digital Filtering

An improvement to the random fluctuations approach, introduced by Klein et al., uses a digital linear non-recursive filtering or convolution approach to create spatial and temporal coherence of the generated turbulence signal (Klein et al., 2003). In the absence of the exact two-point autocorrelation tensor, Klein et al. proposed a Gaussian filter depending on the length scale while other authors favored a proper-orthogonal decomposition (Jarrin et al., 2006). In any case, the digital filtering approach requires extensive knowledge of the upstream flow and the filter coefficients are computationally expensive to obtain (Jarrin, 2008).

Inverse Fourier Transform

Another approach to give some coherence to the generated data is the inverse Fourier transform approach introduced by Lee et al.. It assumes previous knowledge of the spectral densities at the inflow plane and extracts the corresponding Fourier coefficients. The phase of the reconstructed signal is randomly shifted at given time intervals for each wave number to eliminate some of the periodicity implicitly contained in this method (Lee, Lele, & Moin, 1992). However, this approach still contains signs of periodic behavior and becomes very expensive when used with unstructured grids (Jarrin et al., 2006).

Mixed and additional methods

In addition to the previously described methods that act exclusively in physical or spectral space, a variety of methods are available that act in both spaces or rely on forcing terms (source terms) to accelerate transition instead of prescribing an already turbulent inflow plane. These methods are generally not able to overcome the restrictions of their underlying techniques and are limited to specific applications. Therefore, these methods are not covered in this thesis and the reader is referred to a recent paper by Wu (Wu, 2017) for an excellent overview.

2.3.3   Synthetic Eddy Method

The Synthetic Eddy Method (SEM) was initially proposed by Jarrin et al. (Jarrin et al., 2006). It aims to solve to coherence problems of random methods by convecting randomly generated turbulent eddies while keeping computational costs low and remaining suitable for an arbitrary geometry and upstream flow field (Jarrin, 2008).

Numerical Procedure

The underlying principle of the SEM is to follow the classic idea of turbulence in the sense that eddies are structures being convected by the mean flow. Jarrin uses a superposition of these eddies to generate a temporal and spatial coherent signal on the inflow plane which subsequently gets rescaled to match the desired turbulent characteristics (Jarrin et al., 2006).

The following section outlines the SEM on an arbitrary plane in 3-dimensional space by following its description by Sagaut et al. (Sagaut, Deck, & Terracol, 2013). For simplicity, it is assumed that the inlet plane is normal to the mean flow vector, although this is not a requirement of the SEM per se.

The SEM is started by estimating the size of the turbulent structures σ. Jarrin originally proposed σ to be determined by

$$\sigma = max \left(\Delta_{Cell}, \frac{k^{3/2}}{\epsilon} \right) \tag{2.16}$$

where $\epsilon = C_\mu k \omega$ (Jarrin et al., 2006). However, this definition was later adjusted to include the boundary layer thickness δ, to relax the eddy size in areas known to be difficult to resolve in RANS simulations (Sagaut et al., 2013). Therefore, later publications, e.g. (Jarrin, Prosser, Uribe, Benhamadouche, & Laurence, 2009), give σ as

$$\sigma = max \left(min \left[\frac{k^{3/2}}{\epsilon}, \kappa\delta \right], \Delta_{Cell,max} \right) \tag{2.17}$$

where $\Delta_{cell,max}$ corresponds to the maximum local grid size (Sagaut et al., 2013). The maximum eddy size is subsequently used to create a box encompassing the inlet plane and extending $\pm max(\sigma)$ beyond the plane in each direction. The total number of eddies is then calculated as

$$N = max \left(\frac{V_B}{\sigma^3} \right) \tag{2.18}$$
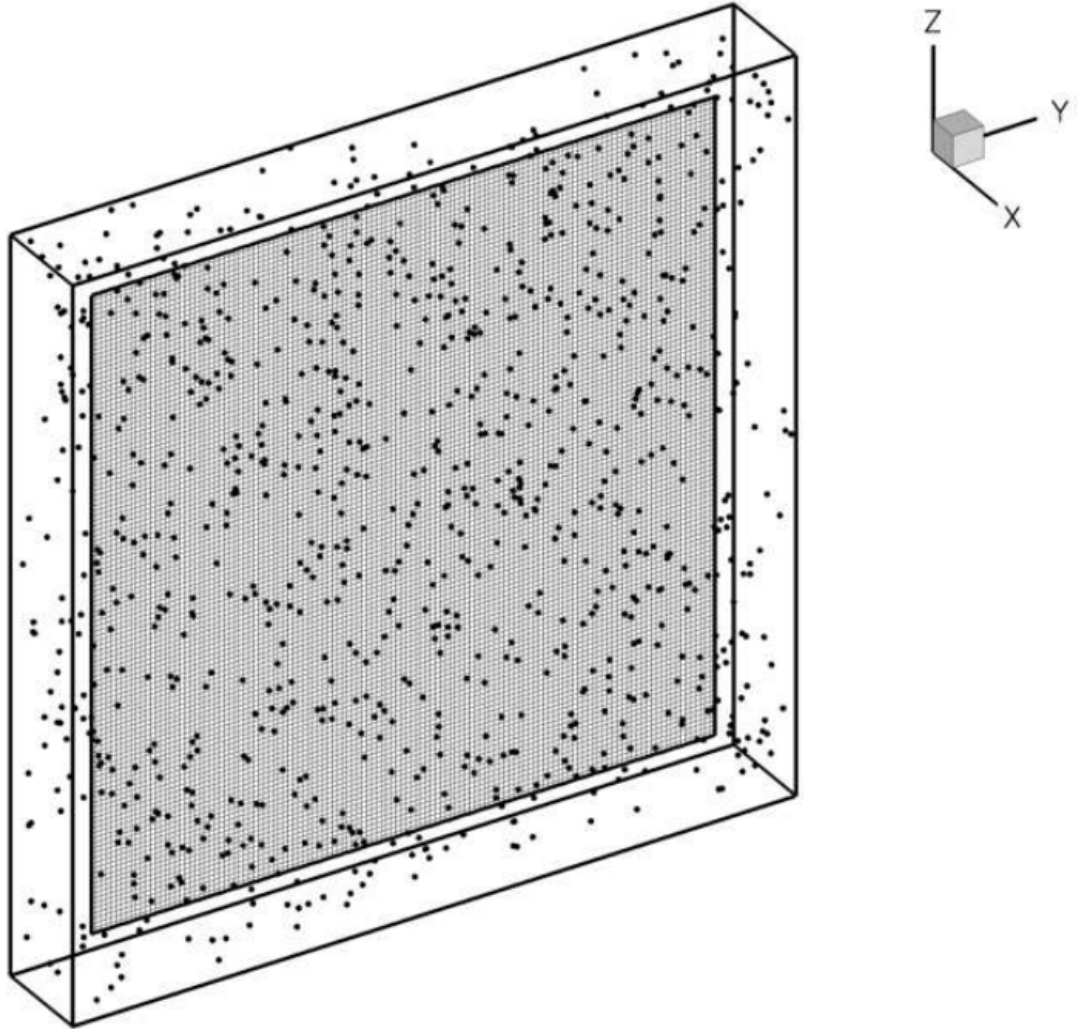
Figure 2.4 Representation of the box encompassing the inlet plane and the inital random distribution of eddies (Jarrin, 2008)

where V_B is the box volume. Initially, the position of each eddy in the box is determined randomly. The contribution of each eddy to the turbulent signal is evaluated by

$$f_\sigma(\mathbf{x} - \mathbf{x}_k) = \sqrt{V_B}\sigma^{-3} f\left(\frac{x - x_k}{\sigma}\right) f\left(\frac{y - y_k}{\sigma}\right) f\left(\frac{z - z_k}{\sigma}\right) \qquad (2.19)$$

where bold symbols denote vector property. The 1D shape function f is given by a tent function defined as

$$f(x) = \begin{cases} \sqrt{\frac{3}{2}}\,(1 - |x|) & x < 1 \\ \\ 0 & \text{otherwise} \end{cases} \tag{2.20}$$

Using eqn. (2.20), the eddies have compact support in $[-\sigma; \sigma]$ and the shape function fulfills the normalization condition $\int_{\mathcal{R}} f^2(x)dx = 1$ (Sagaut et al., 2013). To find the velocity fluctuation at each grid point $\mathbf{x}$, the contributions from the individual eddies are superpositioned as

$$u_i'(\mathbf{x}, t) = \sum_{j=1}^{3} a_{ij} \frac{1}{\sqrt{N}} \sum_{k=1}^{N} \epsilon_k^j f_{\sigma_j}(\mathbf{x} - \mathbf{x_k}(t)) \tag{2.21}$$

where $i = 1, 2, 3$ corresponds to the coordinate axes, a_{ij} is the Cholesky decomposition of the Reynolds stress tensor and ϵ_k^j is the sign of eddy k which is randomly chosen between -1 or $+1$. While Jarrin et al. and Sagaut et al. stop here, it is revealing to combine eqn. (2.19) and (2.21) to

$$u_i'(\mathbf{x}, t) = \sum_{j=1}^{3} a_{ij} \frac{[min(\sigma)]^3}{\sigma^3} \sum_{k=1}^{N} \epsilon_k^j f_{\sigma_j}(\mathbf{x} - \mathbf{x_k}(t)) \tag{2.22}$$

which shows that the velocity fluctuation strength is determined exclusively by the Cholesky decomposition, the shape function and the ratio between the local and the minimum eddy size. For any positive definite symmetric matrix $\mathbf{A}$, including the Reynolds stress tensor, the Cholesky factorization is fulfilled if the matrix $\mathbf{R}$ is an upper triangular matrix and

$$\mathbf{A} = \mathbf{R}^T \mathbf{R} \tag{2.23}$$

It was shown by Lund et al. (Lund et al., 1998) that these conditions are fulfilled if the components a_{ij}, the Lund coefficients (Poletto, Craft, & Revell, 2013), for the Cholesky decomposition of the tensor $\mathbf{R}$ are chosen as

$$
a_{ij} = \begin{bmatrix} \sqrt{R_{11}} & 0 & 0 \\ R_{21}/a_{11} & \sqrt{R_{22} - a_{21}^2} & 0 \\ R_{31}/a_{11} & (R_{32} - a_{21}a_{31})/a_{22} & \sqrt{R_{33} - a_{31}^2 - a_{32}^2} \end{bmatrix} \tag{2.24}
$$

2.3.4 Modifications to the original Synthetic Eddy Method

Divergence-free Condition

The SEM as prescribed above is able to reproduce any desired (anistropic) Reynolds stress field. However, because the velocity fluctuations are based on an isotropic signal, the produced velocity field will in general not be divergence-free (Poletto et al., 2013). Poletto et al. proposed a modification of Jarrin's SEM which transforms the Reynolds stress tensor into the local principal coordinate system where an anisotropic length-scale for the eddies can be prescribed (Poletto, Revell, Craft, & Jarrin, 2011). The original SEM was later modified by Poletto et al. (Poletto et al., 2013) to incorporate the anistropic length-scale by expressing r^k as

$$
r_\beta^k = \frac{\mathbf{x}_\beta - \mathbf{x}_\beta^k}{\sigma_\beta^k} \tag{2.25}
$$

from which the turbulent fluctuations at any point of the plane can be derived as

$$
u_\beta' \mathbf{x} = \sqrt{\frac{1}{N} \sum_{k=1}^{N} q_\beta \left(\mathbf{x}, \mathbf{x}^k, \sigma^k \right) \epsilon_{\beta jl} r_j^k \alpha_l^k} \tag{2.26}
$$

where $\epsilon_{\beta jl}$ denotes the Levi-Civita symbol. Setting $d^k = \sqrt{(r_j^k)^2}$, the shape function is given by

$$q_i = \begin{cases} \sigma_i \left[1 - (d^k)^2 \right] & d^k < 1 \\ \\ 0 & \text{otherwise} \end{cases} \tag{2.27}$$

As this formulation describes the Reynolds stresses in the principal coordinate system, the generated field is strictly diagonal and has to be rotated back to the computational coordinate system via the local transformation matrix to recover shear stresses. The reader is referred to the original paper for the complete formulation.

Poletto et al. claims this divergence-free formulation reduces pressure fluctuations near the inlet and results in a shorter development length (Poletto, Revell, & Craft, 2012; Poletto et al., 2013). While his published results are impressive and OpenFOAM Ltd announced the implementation of this method in the current OpenFOAM-plus release (OpenCFD Ltd, 2016), Poletto's results could not be reproduced using the currently available versions of OpenFOAM-plus and Code_Saturne. Furthermore, a request for more information has been declined by the author of the DFSEM paper. Given the density-based formulation of the Eagle3D solver, the benefit of a divergence-free formulation would be uncertain, so the original formulation by Jarrin was implemented in this thesis work.

Energy Equation

Previous implementations of the SEM were developed for pressure-based solvers, most notable among them OpenFOAM and Code_Saturne (Jarrin et al., 2006; Poletto

et al., 2013) which connect the pressure-field to the reconstructed fluctuating velocity field through a Poison equation and use the incompressibility assumption to neglect the energy equation. Therefore, the entire turbulent kinetic energy can be expressed by just the velocity fluctuations.

For a density-based solver such as Eagle3D, the system obtained from the Navier-Stokes equations includes the energy equation. To ensure correct representation of the turbulent fluctuations, the instantaneous field should be defined for the static temperature in addition to velocity. A simple approach is to specify the static temperature on the inlet by assuming stagnation temperate is held constant. This assumptions is valid near the inlet plane of a low speed subsonic flow. Then, the static temperature is given by

$$T = \frac{T_0 + \sqrt{T_0^2 + 2\frac{u^2}{cp}}}{2} \tag{2.28}$$

However, resulting changes in static temperature are on the order of $10^{-5}\,K$ for the low speed subsonic cases explored herein. While this effect will become more noticeable for high speed flows, a constant static temperature was assumed in the inlet for all test cases.

Mass Flow Fluctuations

Poletto et al. (Poletto et al., 2011) noted that instantaneous bulk flow rate through the SEM inflow plane varies compared to the constant upstream RANS solution as the sum of the fluctuations is usually non-zero. While the effect of this flow rate variation

is usually negligible for free-stream cases, it leads to pressure waves propagating in the streamwise direction for wall-bounded internal flows. His solution is a rescaling of the bulk flow rate through the inlet with

$$c_{rescale} = \frac{\sum_{i=1}^{N}(u_{mean,i} + u_i') \cdot A_n}{\sum_{i=1}^{N} u_{mean,i} \cdot A_n} \tag{2.29}$$

$$u = \frac{u_{mean,i} + u_i'}{c_{rescale}} \tag{2.30}$$

where N denotes the number of faces on the inlet plane. The maximum deviation of $c_{rescale}$ from uniform was observed to be less then 1% for all test cases, which matches Poletto et al. results. Therefore, the overall influence of the rescaling on the turbulent statistics can safely be neglected. This rescaling is utilized in the present work.

Multi-Layer SEM

Eagle3D as a high-order CFD solver relies on multiple upstream ghost cells at the inlet, specifically 3 ghost cells are needed for the 5th order WENO scheme. The classic SEM was derived with 2nd order accurate schemes in mind and does not account for high-order schemes. It was speculated that a multi-layer formulation of the SEM might be able to give more accurate values for the underrepresented streamwise and wall-normal components of vorticity. The multi-layer formulation expands the eddy box in negative x-direction and extracts values at $x = -2\Delta_{cell,x}$ and $x = -\Delta_{cell,x}$ in addition to the standard plane at $x = 0$ to give approximations of the turbulent fluctuations for all 3 ghost cells.

3. Test Case Configurations

The flow over a cylinder was simulated and compared to ANSYS Fluent to confirm the ability of Eagle3D to give accurate results for unsteady turbulent flows. Two test cases, the fully turbulent channel flow and the flow over a flat plate, were chosen to verify the ability of the implemented SEM to reproduce a given Reynolds stress profile as well as to start a realistic turbulent behavior in the Eagle3D solver. Both test cases employed only low-speed subsonic flow to demonstrate the performance of this code combination in a flow regime usually occupied by pressure-based CFD solvers. All simulations used air as medium with internal conditions given in tab. 3.1 unless explicitly stated otherwise.

Table 3.1. Used internal conditions for air as fluid medium

Quantity	Symbol	Magnitude	Unit
Static Temperature	T	300	K
Density	ρ	1.18	$\frac{kg}{m^3}$
Kinematic Viscosity	ν	$1.525 \cdot 10^{-5}$	$\frac{m^2}{s}$

3.1   Flow over a Cylinder

Performance of the TBD solver which eventually turned into Eagle3D has already been demonstrated by comparison against experimental data and NASA's Wind CFD solver for high-speed multi-specie RANS flow by Engblom et al. (Engblom et al., 2007). To demonstrate Eagle3D's ability to perform well in low-speed LES simulations, the unsteady flow over a cylinder was chosen.

3.1.1   Mesh

The cylinder case used a $0.0165\,m$ cylinder in a $0.2286 \times 0.08 \times 0.07\,m$ domain, simulated by a fully structured 3D mesh with $815 \times 356 \times 32$ cells on the domain boundaries. The region close to the cylinder was split into 4 equiangular quadrants and refined with $1,420,064$ cells each, resulting in a total of $13,100,896$ cells.

3.1.2   Boundary Conditions

Mean flow boundary conditions are summarized in tab. 3.2 with the reference pressure neglected for the pressure-based Fluent case. The wall of the cylinder was set to be a fully adiabatic wall, the outflow and the top and bottom side a pressure-outlet and the front and back to be periodic conditions.

These boundary conditions together with the geometric dimensions from sec. 3.1.1 result in a Reynolds number based on cylinder diameter as

$$Re_d = \frac{U_\infty d}{\nu} = 9735 \tag{3.1}$$

Table 3.2. Boundary conditions for the cylinder flow case

Patch	Quantity	Symbol	Magnitude	Unit
Inlet	Velocity	U	9	$\frac{m}{s}$
	Temperature	T	300	K
Outlet	Static pressure	p	10^6	Pa
Cylinder Wall	Wall velocity	U_{wall}	0	$\frac{m}{s}$

Flow past a cylinder with $300 < Re_d < 3 \cdot 10^5$ is expected to form a fully turbulent vortex street (Blevins, 1990) with a Strouhal number of

$$St = \frac{fd}{U_\infty} \approx 0.20 \tag{3.2}$$

for $Re_d \simeq 10,000$. Vortex shedding frequency is then given as

$$f = \frac{StU_\infty}{d} = 109.1 \, Hz \tag{3.3}$$

and confirmed by an animation of the LES results.

3.1.3   Models, Interfaces and Settings

The density-based compressible Eagle3D code was run using the 2nd order BCD scheme coupled with a 5th order WENO scheme (see sec. 2.1.2). ANSYS Fluent was configured to utilize a 2nd order pressure-based, incompressible SIMPLEC solver combined with bounced central differencing on the momentum flux terms.

3.2 Fully Turbulent Channel Flow

The fully turbulent channel flow is one of best studied cases and often used as a reference because the mean flow properties in the fully turbulent case do not depend on downstream distance, therefore, the mean flow becomes self-similar. This self-similarity allows for an reliable analysis of the SEM's ability to reproduce the upstream profile and a measurement of the development length to recover the original stresses.

3.2.1 Mesh

The mesh used originally for the channel flow case (hereinafter called `CHAN1`) is a fully rectangular hexahedral mesh with $46 \times 82 \times 500$ cells, resulting in a total of $1,886,000$ cells. It was created in Pointwise with all dimensions and the geometric growth rate identical to the mesh used in the OpenFOAM tutorial case for their DFSEM method as well as by Poletto (Poletto et al., 2013) in Code_Saturne.

In addition to this mesh, a refined version was tested with $100 \times 100 \times 500$ cells and a more traditional $tanh$ growth rate, resulting in a mesh with $5,000,000$ cells and designated `CHAN2`. Both meshes share identical wall cell spacing corresponding to a $y^+ = 1$ and had the dimensions of $2 \times \pi \times 20\pi\, m$.

3.2.2 Boundary Conditions

Data from Direct Numerical Simulation (DNS) at various friction Reynolds Re_τ numbers ranging from 180 to 590 based on friction velocity Re_τ is provided by Moser et al. (Moser, Kim, & Mansour, 1999). For this thesis, the profiles corresponding to $Re_\tau = 395$ for channel half width $\delta = 1\,m$ were selected. Corresponding profiles by Moser et al. are shown in fig. 3.1 and mean flow boundary conditions are summarized in tab. 3.3.

(a) Axial velocity profile   (b) Reynolds normal stresses profile
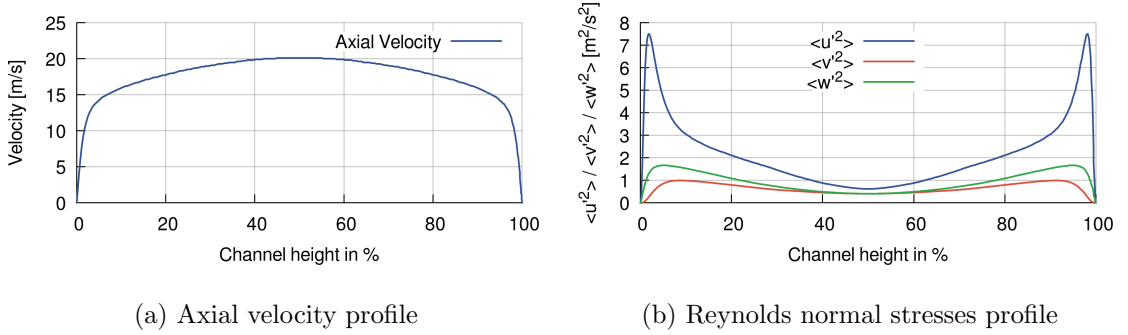
Figure 3.1 Profiles for axial velocity and Reynolds normal stresses at the inlet corresponding to $Re_\tau = 395$ (Moser et al., 1999)

To ensure compatibility of the bulk flow velocity and wall velocity gradient $\left.\frac{\delta U}{\delta y}\right|_{y=0}$ $= 392.24\frac{1}{s}$ with the given friction Reynolds number, the kinematic viscosity ν had to be adjusted by

$$\tau_w \equiv \rho\nu \left.\frac{\partial U}{\partial y}\right|_{y=0} \tag{3.4}$$

$$u_\tau \equiv \sqrt{\frac{\tau_w}{\rho}} \tag{3.5}$$

$$Re_\tau \equiv \frac{u_\tau \delta}{\nu} \tag{3.6}$$

Table 3.3. Boundary conditions for the channel flow case

Patch	Quantity	Symbol	Magnitude	Unit
Inlet	Bulk Velocity	U_{bulk}	17.5474	$\frac{m}{s}$
	Temperature	T	300	K
Outlet	Static pressure	p	10^6	Pa
Walls	Wall velocity	U_{wall}	0	$\frac{m}{s}$

therefore

$$\nu = \frac{\delta^2 \left.\frac{\partial U}{\partial y}\right|_{y=0}}{Re_\tau{}^2} = 2.51395 \cdot 10^{-3} \frac{m^2}{s} \tag{3.7}$$

This viscosity is considerably higher than the expected value of air. The entire flow field was initialized with the steady-state RANS solution given at the inlet. Given their natures as LES meshes, both grids are unable to recover the exact DNS resolution via LES. Instead, an approach similar to Poletto et al. was taken which uses the DNS data as inflow conditions, but evaluates the SEM on the ability to recover values as would be expected from a recycling (periodic) LES. Independent empirical and DNS studies agree on a theoretical $C_{f_b} = 0.0064 - 0.0069$ for $Re_\tau \approx 390$ (Dean, 1978; Moser et al., 1999; Alfonsi, Ciliberti, Mancini, & Primavera, 2016) with C_{f_b} defined as

$$C_{f_b} = \frac{\tau_w}{\frac{1}{2}\nu U_{bulk}^2} \tag{3.8}$$

Using the proposed `CHAN1` grid, Poletto et al. stated a $C_{f_b} = 0.0032$ as the value to be expected from periodic LES with 2nd order schemes in Code_Saturne (Poletto et

al., 2013) which matches with other LES publications such as Schiavo et al. (Schiavo, de Jesus, Wolf, & Azevedo, 2013).

3.2.3   Models, Interfaces and Settings

Each simulation was assigned a unique identifier to differentiate the results. The first potion of the identifier states the mesh (i.e., `CHAN1` for the course grid, `CHAN2` for the fine grid). It is followed by the method used for subgrid treatment, either fully implicit LES (i.e., `ILES`) or a LES utilizing the Smagorinsky subgrid model (i.e., `SGM`). Subsequently, the simulations are distinguished by the number of upstream ghost cells provided by the SEM (i.e., `1-3`). Finally, the eddy length scale is given in percentage of the channel half width δ (i.e., `15-40`). The only exclusion is the `CHAN1.ILES.1.6c` case which set the length scale grid dependent as $6 \cdot \max(\Delta_{cell})$. Tab. 3.4 contains a breakdown for all channel flow simulations performed for this thesis.

The Smagorinsky-Lilly model used a conservative approach, estimating the added eddy viscosity on the low side by defining the local cell dimension Δ as

$$\Delta = V_{cell}^{\frac{1}{3}} \tag{3.9}$$

and choosing the Smagorinsky constant to the minimal agreed value as $C_s = 0.1$.

Table 3.4. Identifiers for fully turbulent channel flow

Identifier	Channel Case	SGS model	Ghost Cells	Length Scale
CHAN1.ILES.1.6c	Channel 1	Implicit LES	1	$6 \cdot \max(\Delta_{Cell})$
CHAN1.ILES.3.25	Channel 1	Implicit LES	3	$25\% \, \delta$
CHAN2.ILES.1.15	Channel 2	Implicit LES	1	$15\% \, \delta$
CHAN2.ILES.1.25	Channel 2	Implicit LES	1	$25\% \, \delta$
CHAN2.ILES.3.25	Channel 2	Implicit LES	3	$25\% \, \delta$
CHAN2.ILES.1.40	Channel 2	Implicit LES	1	$40\% \, \delta$
CHAN2.SGM.1.15	Channel 2	Smagorinsky	3	$15\% \, \delta$
CHAN2.SGM.1.25	Channel 2	Smagorinsky	3	$25\% \, \delta$

3.2.4   Time Step and Convergence Monitoring

All channel flow test cases were performed with a time step $dt = 5 \cdot 10^{-4} \, sec$. Residuals per subiteration were required to reduce by a minimum of 3 orders of magnitude at the end of the subiteration loop compared to the first subiteration. A maximum of 14 subiterations was permitted per time step and proofed sufficient for the above requirement. Data collection and averaging started after 5.59 flow through periods calculated with the average flow velocity and ended after 8.38 periods.

3.3 Flow over a Flat Plate

The flow over a flat plate is another well studied case which produces a self-similar solution for the mean boundary layer profile if scaled by the boundary layer thickness. For this thesis, a ZLES setup with an upstream 2D RANS mesh followed by a 3D LES grid was chosen.

3.3.1 Mesh

The upstream RANS solutions are produced using the same $208,896$ cell 2D mesh in OpenFOAM-plus and ANSYS Fluent. The former approximated turbulent behavior with an isotropic 2-equation Shear-Stress-Transport (SST) model while the latter utilized the anisotropic 5-equation Wilcox-Stress-Baseline (BSL). Both upstream RANS profiles were extracted at $x = 0.8\,m$ downstream distance from the inlet.

The mesh used for the LES simulations in Eagle3D discretized a $0.75 \times 0.024 \times 0.1\,m$ domain with $2,499 \times 64 \times 198$ cells, resulting in a total of $31,667,328$ cells. The mesh was refined in the expected boundary layer region with 149 cells below $y = 0.02735\,m$ in wall-normal direction, $y^+ = 1$, $dx^+ = 11$ and $dz^+ = 15$.

3.3.2 Boundary Conditions

The boundary conditions for both RANS cases were set according to tab. 3.5. The flat plate was set to be a fully adiabatic wall, the top a pressure-outlet to eliminate

pressure spikes from the growing turbulent boundary layer and the vertical sides using periodic conditions.

Table 3.5. Boundary conditions for the flat plate RANS case

Patch	Quantity	Symbol	Magnitude	Unit
Inlet	Free-stream Velocity	U_∞	10	$\frac{m}{s}$
	Temperature	T	300	K
Outlet	Static pressure	p	10^6	Pa
Walls	Wall velocity	U_{wall}	0	$\frac{m}{s}$

The extracted RANS profiles were used as input for the SEM to reconstruct the turbulent fluctuations at the inflow plane of the LES mesh. Profiles for axial velocity and Reynolds normal stresses are given in fig. 3.2 for the SST model and fig. 3.3 for the BSL model while the remaining boundary conditions are summarized in tab. 3.6. In order to save computational power and memory space, the SEM was restricted to the approximated boundary layer height at $y = 0.02735\,m$. The entire flow field was initialized with the steady-state RANS solution given at the inlet.
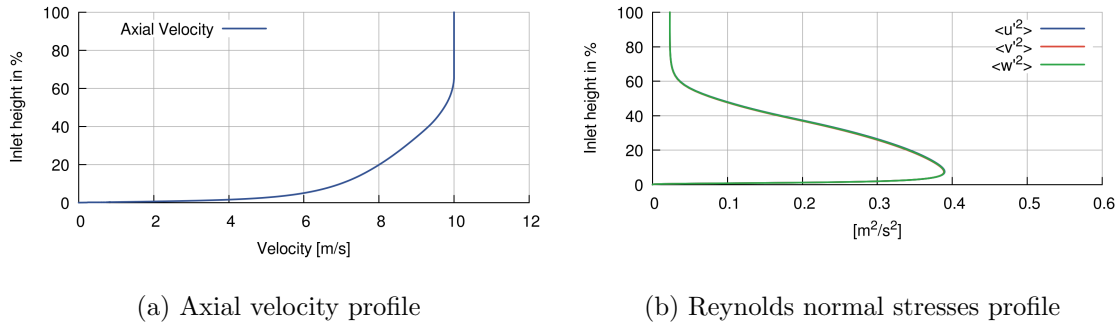
(a) Axial velocity profile

(b) Reynolds normal stresses profile

Figure 3.2 Profiles for axial velocity and Reynolds normal stresses from the SST model at the SEM inlet plane of the flat plate LES mesh

(a) Axial velocity profile
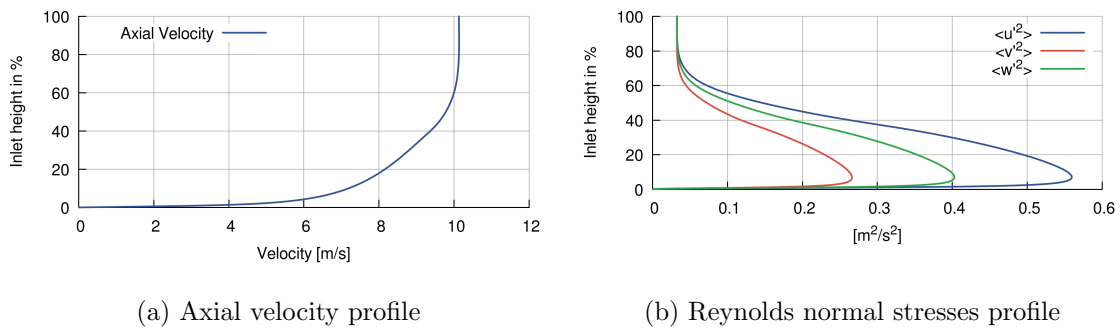
(b) Reynolds normal stresses profile

Figure 3.3 Profiles for axial velocity and Reynolds normal stresses from the BSL model at the SEM inlet plane of the flat plate LES mesh

Skin friction coefficient was defined with the free-stream velocity as

$$C_{f_f} = \frac{\tau_w}{\frac{1}{2}\nu U_\infty^2} \tag{3.10}$$

with the upstream solution giving an expected skin friction coefficient at the inlet of $C_{f_f} = 0.003718$ for $Re_\theta = 1450$ (SST model) to $C_{f_f} = 0.003885$ for $Re_\theta = 1410$ (Schlatter & Örlü, 2011).

Table 3.6. Boundary conditions for the flat plate LES case

Patch	Quantity		Symbol	Magnitude	Unit
	Free-stream Velocity		U_∞	10	$\frac{m}{s}$
Inlet	Bulk Velocity	SST	U_{bulk}	8.9315	$\frac{m}{s}$
		BSL	U_{bulk}	9.0884	$\frac{m}{s}$
	Temperature		T	300	K
Outlet	Static pressure		p	10^6	Pa
Walls	Wall velocity		U_{wall}	0	$\frac{m}{s}$

3.3.3 Time Step and Convergence Monitoring

All flat plate test cases were performed with a time step $dt = 5 \cdot 10^{-6}\,sec$. Residuals per subiteration were required to reduce by a minimum of 3 orders of magnitude at the end of the subiteration loop compared to the first subiteration. A maximum of 14 subiterations was permitted per time step and proofed sufficient for the above requirement. Data collection and averaging started after 1.21 flow through periods calculated with the average flow velocity and ended after 2.42 flow through periods.

3.4 Other CFD solvers

The focus of this thesis is to determine the ability of Eagle3D in conjunction with the SEM to accurately simulate the given test cases. Other CFD codes were used

to provide data for comparison where no analytic or DNS data is available. These solvers were also used to provide upstream RANS data for the flat plate test case.

3.4.1 OpenFOAM-plus

The Open Source Field Operation And Manipulation (OpenFOAM) is a free-to-use toolbox and one of the most used CFD environments today. Its source is written in C++ and released under the GNU General Public License by The OpenFOAM Foundation. OpenFOAM provides complete functionality of the CFD process, including meshing, pressure- and density-based simulation, pre- and post-processing. Beginning with OpenFOAM 3.0, OpenCFD Ltd. (ESI Group) started publishing their variant of OpenFOAM, named OpenFOAM-plus. OpenFOAM-plus is released semi-annually and resynced to OpenFOAM at the beginning of a new development cycle. This allows OpenFOAM-plus to stay mostly compatible with the upstream code base while adding bleeding-edge features. For this thesis, OpenFOAM-plus was used in v1606+.

3.4.2 ANSYS Fluent

ANSYS Fluent is a CFD toolbox developed and distributed by the US-based company ANSYS, Inc. It has found wide acceptance throughout academia as well as the industry for its highly optimization and reliable performance. However, because its closed source the underlying numerical methods cannot be checked or modified

with exception of user defined functions (UDF) for boundary conditions. For this thesis, ANSYS Fluent was used in version 17.

4. Results

Simulations were either performed on Embry-Riddle Aeronautical University's Vega cluster or on NASA's Pleiades computer. Both systems utilize a distributed resource manager to share and schedule resources. Channel flow simulations were run on 200 CPU cores in parallel on Vega while the flat plate cases utilized 400 cores on Pleiades.

4.1 Flow over a Cylinder

A common indicator of turbulent structures is the Q criterion, first defined by Hunt et al. (Hunt, Wray, & Moin, 1988) as the second invariant of the velocity gradient tensor

$$Q = \frac{1}{2} \left[(\mathrm{tr}\,(\nabla u))^2 - \mathrm{tr}\,(\nabla u \cdot \nabla u) \right] \tag{4.1}$$

with tr denoting the trace. Eddies can be identified using Q isosurfaces. Comparisons of streamwise velocity and Q criterion for the flow over a cylinder in ANSYS Fluent and Eagle3D are shown in fig. 4.1 and fig. 4.2, respectively. The simulations were run on with different time steps due to different time advancement schemes.

Despite ANSYS Fluent using a pressure-based, 2nd order bounded central differencing approach and Eagle3D utilizing a density-based, high-order BCD method, both figures show good qualitative, and to some extent quantitative, agreement. Overall
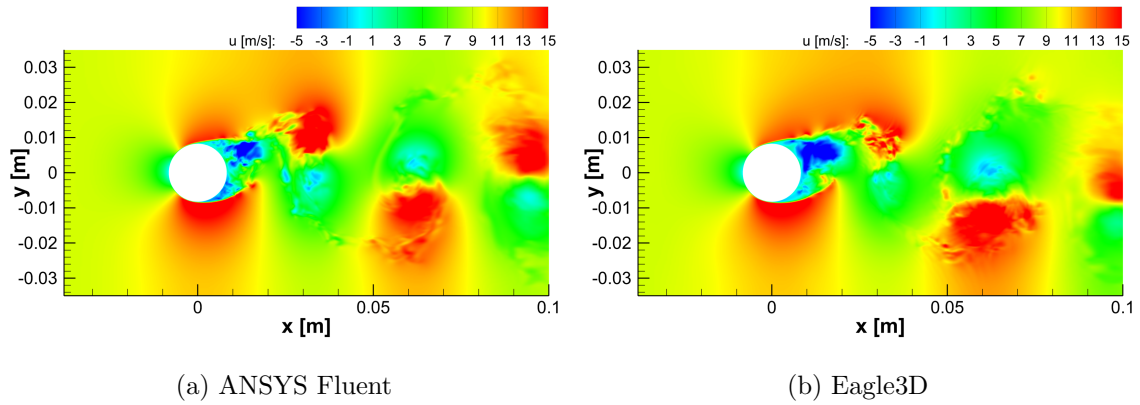
(a) ANSYS Fluent

(b) Eagle3D

Figure 4.1 Comparison of streamwise velocity of the cylinder flow case in ANSYS Fluent and Eagle3D

flow pattern in the velocity plots match, with similar position and magnitude of extremas. The 5th-order Eagle3D solver shows higher fidelity in certain areas, most noticeable in the forming vortex immediately after the cylinder and the second detached vortex moving in positive y-direction.
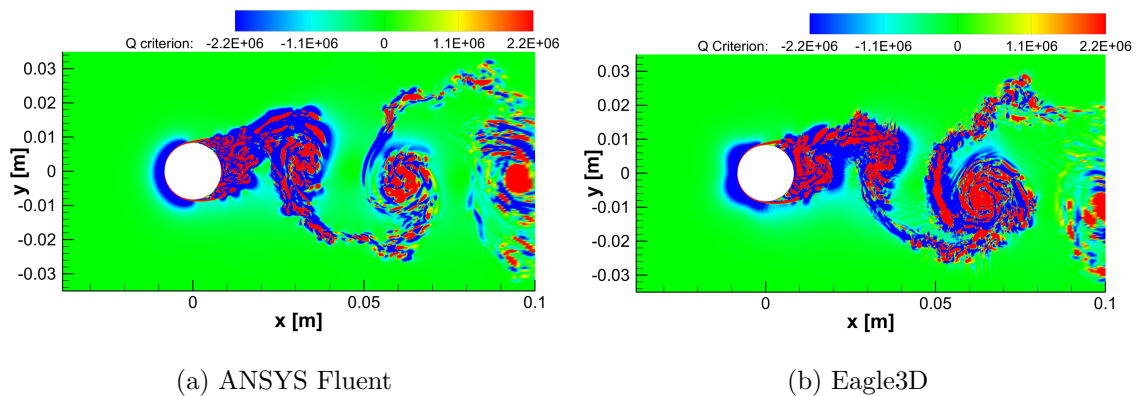

(a) ANSYS Fluent

(b) Eagle3D

Figure 4.2 Comparison of Q criterion of the cylinder flow case in ANSYS Fluent and Eagle3D

Comparison of Q criterion emphasizes the ability of Eagle3D to produce reliable LES results. Vortex position and movement in Eagle3D are comparable to results

from ANSYS Fluent. Results from Eagle3D show higher overall resolution, most obvious for the downward moving part of the vortex at $x \approx 0.05\,m$. Average values of Q criterion produced by Eagle3D are higher than ANSYS Fluent, resulting in "fuller" vortices, which is partly expected when considering the higher fidelity of Eagle3D. Stronger oscillations of Eagle3D can be observed at the forward facing part of the cylinder while these oscillations are more damped out by ANSYS Fluent.

4.2 Fully Turbulent Channel Flow

All simulations were performed in the Eagle3D CFD solver with the SEM running separately as a precursor simulation. Plots marked as "SEM" refer to this combination if not mentioned otherwise. Wall shear stress coefficient C_{f_b}, velocity components, and Reynolds stresses, are spanwise averaged over $20,000$ iterations when reporting statistics to smooth out the effects of unsteady turbulent fluctuations.

4.2.1 Convergence and Computation Time

Computational time for $10,000$ iterations in the `CHAN2` simulation split into SEM and Eagle3D is given in tab. 4.1. The SEM in single-layer formulation is able to fulfill the requirement to produce turbulent fluctuations in less than $5\,\%$ of the computational time needed for the main simulation while the multi-layer version (to be described later) has higher computational demands and stays just under $10\,\%$ of total

simulation time. However, both codes were partly limited in their performance by

I/O operations as tests with disabled output produced faster runtimes.

Table 4.1. Time requirements for $10,000$ iterations in SEM and Ea-
gle3D for the `CHAN2` case with 200 CPU cores on Embry-Riddle's Vega
cluster

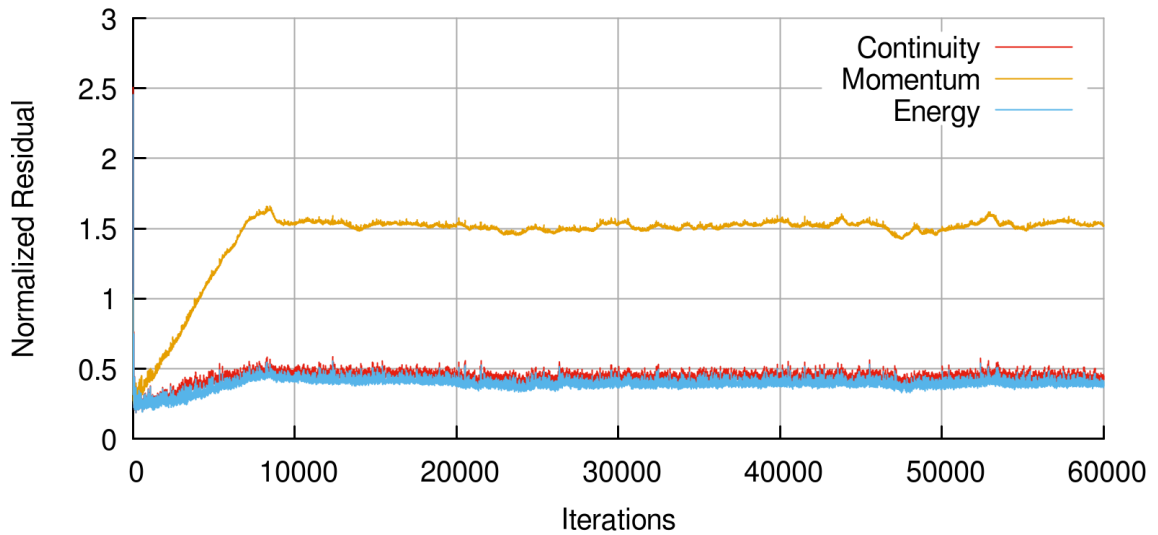| Simulation	# of Ghost Cells	Real Time for $10,000$ Iterations
Single-Layer SEM	1	$11\,min$
Multi-Layer SEM	3	$47\,min$
Eagle3D	–	$581\,min$

Figure 4.3 Residual curves for the fully turbulent channel flow

Residual curves for all fully turbulent channel flow simulations show satisfactory

behavior with an exemplary plot given in fig. 4.3. Residuals are normalized against

the value of the first iteration which corresponds to the RANS initialization. There-
fore, residuals can converge at values higher than unity once the simulation becomes
fully unsteady LES.

4.2.2   Reproduction of Reynolds Stresses

A prominent feature of the SEM is the ability to reproduce an unsteady turbulent
velocity field from an arbitrary Reynolds stress distribution given by RANS or time-
averaged DNS data. Comparison of DNS data by Moser (Moser et al., 1999) and the
Reynolds normal stress profile generated by the SEM for the `CHAN1.ILES.1.15` case
is given in fig. 4.4. The SEM shows excellent agreement with the DNS data despite
visible aliasing from the lower resolution of the inlet mesh.
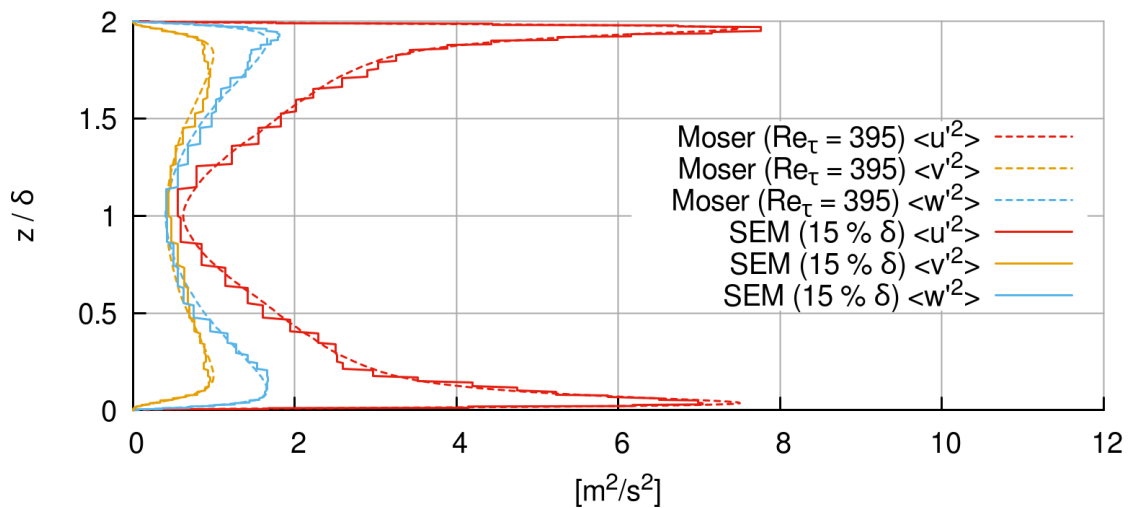

Figure 4.4 Comparison of Reynolds normal stresses generated by the
SEM with DNS results by Moser (Moser et al., 1999)

4.2.3   Initialization of Turbulent Behavior

Fig. 4.5 and fig. 4.6 show C_{f_b} and axial velocity as well as Reynolds normal stresses, respectively. Comparison of the wall shear stress coefficient C_{f_b} with the analytic solution confirms that the outlet is still within the development length of the SEM for both cases. Earlier publications by Poletto et al. concur on the need for a development length, but limit its extent to usually $30\,\delta$ (Poletto et al., 2013). Values for C_{f_b} at the outlet are lower than $C_{f_b} = 0.0032$ reported by Poletto for periodic LES (Poletto et al., 2013) despite the higher order of Eagle3D compared to 2nd order schemes in Code_Saturne.

(a) Wall shear stress coefficient C_{f_b} (b) Axial velocity
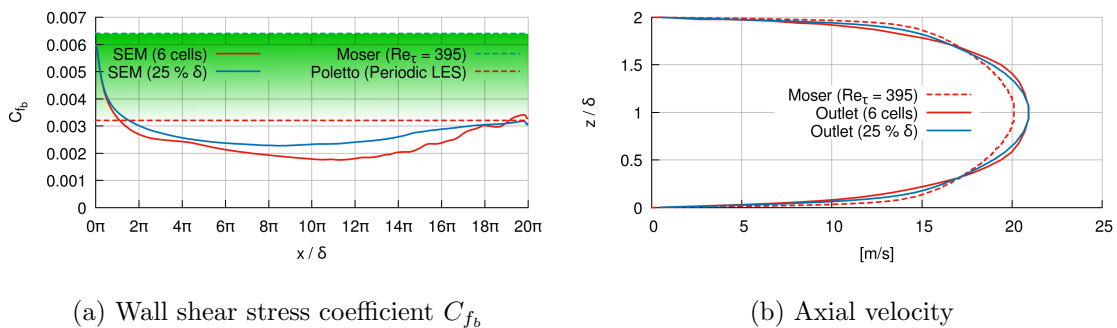
Figure 4.5 Comparison of wall shear stress coefficient C_{f_b} and axial velocity in the CHAN1.ILES.1/3.6c/15 case with DNS results by Moser (Moser et al., 1999) and LES results by Poletto (Poletto et al., 2013)

The wall velocity gradient in fig. 4.5b corresponds to a friction Reynolds number $Re_\tau = 258$ for the CHAN1.ILES.1.6c case and $Re_\tau = 277$ for the CHAN1.ILES.3.25 case and confirms the ability of the SEM to start turbulent behavior in the turbulent channel flow. However, both friction Reynolds numbers are significantly lower than expected from the upstream solution with $Re_\tau = 395$.
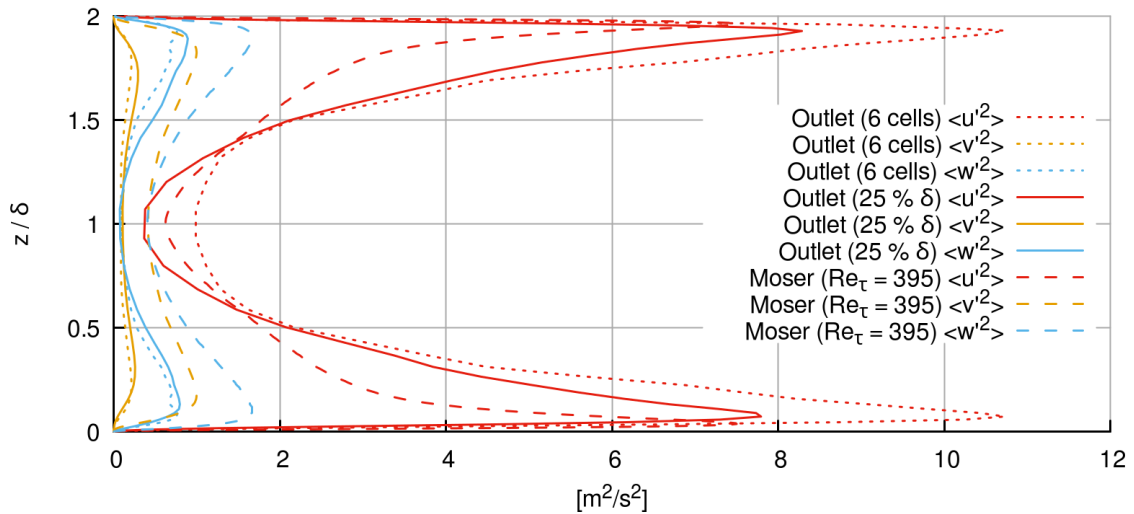
Figure 4.6 Comparison of Reynolds normal stresses of CHAN1.ILES.1/3.6c/15 with DNS results by Moser (Moser et al., 1999)

Comparison of Reynolds normal stresses of both cases in fig. 4.6 with DNS data by Moser (Moser et al., 1999) shows individual components match the expected order with $\langle u'^2 \rangle > \langle w'^2 \rangle > \langle v'^2 \rangle$. Quantitatively, streamwise turbulence in the near-wall region is overpredicted while spanwise and wall-normal components are underestimated. Qualitatively, the data appears underresolved with the effect most visible in the $\langle u'^2 \rangle$ component where the grid is apparently unable to reproduce the steep gradients near the wall.
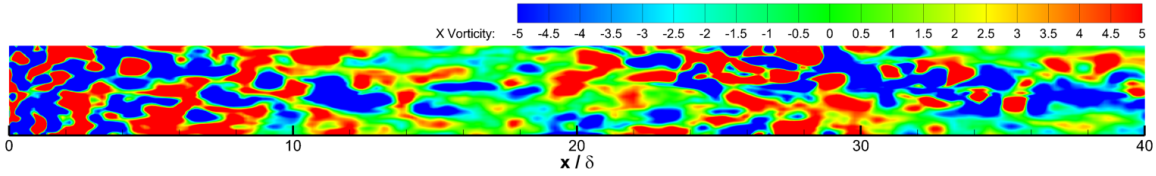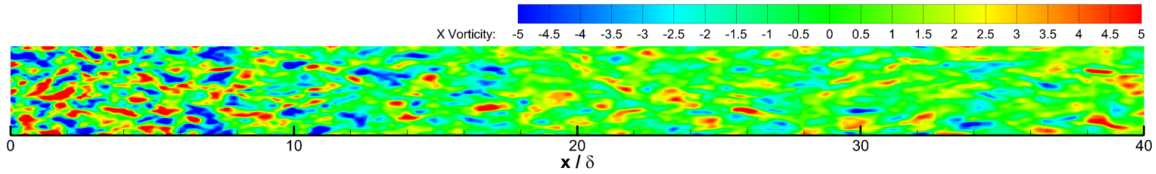
(a) $z/\delta = 0.05$ slice

(b) $z/\delta = 1$ slice

Figure 4.7 Streamwise component of instantaneous vorticity in the CHAN1.3.ILES.25 case at wall parallel planes at $z/\delta = 0.05$ and $z/\delta = 1$

Qualitative analysis of the streamwise component of instantaneous vorticity at two slices parallel to the wall in fig. 4.7 affirms the prolonged development length. Overall magnitude of x-vorticity drops within $10\,\delta$ after the inlet and is not fully recovered by the end of the channel. Additionally, turbulent structures near the wall appear enlarged by orders of magnitude compared to expected pattern at this position. Due to the insufficient resolution of the CHAN1 grid, all further turbulent channel flow simulations were performed on the CHAN2 grid. Eddy length scale was fixed to a percentage of the channel half width δ to provide a grid-independent specification.

4.2.4   Influence of Eddy Length Scale Parameter

Mesh refinement from 1.886 million cells (`CHAN1`) to 5 million cells (`CHAN2`) resulted in significant improvements. Fig. 4.8 gives a comparison of the wall shear stress coefficient C_{f_b} for a length scale ranging from $15\%\,\delta$ to $40\%\,\delta$.
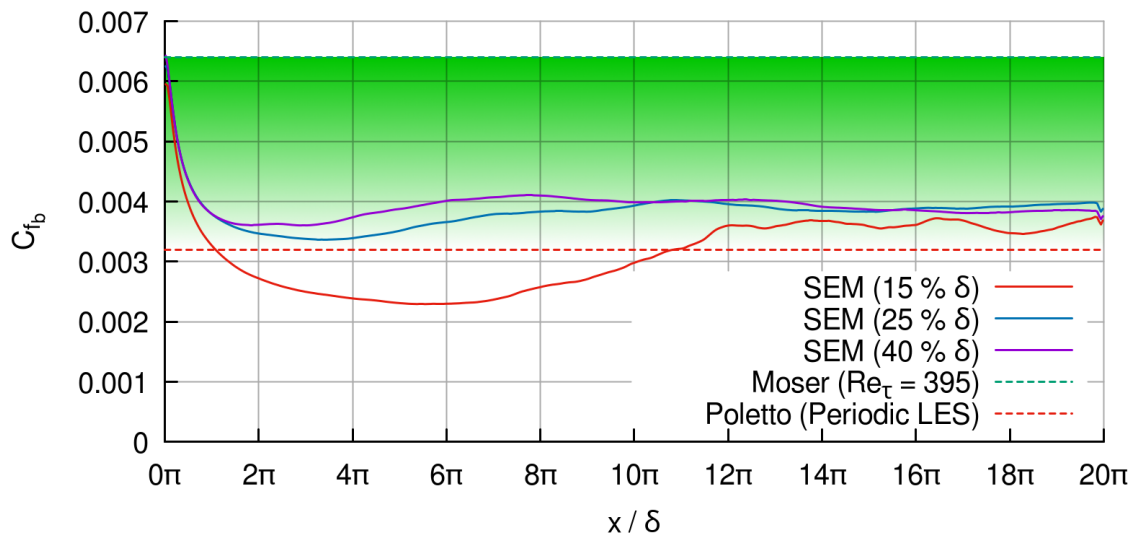

Figure 4.8 Comparison of wall shear stress coefficient C_f in the `CHAN2.ILES.1.15-40` cases with DNS results by Moser (Moser et al., 1999) and LES results by Poletto (Poletto et al., 2013)

All cases tend to an value of $C_{f_b} \approx 0.0038$ which is slightly higher than the $C_{f_b} = 0.0032$ reported by Poletto's periodic LES (Poletto et al., 2013), showing Eagle3D's ability to take benefit of both higher-order schemes and a finer mesh. The smaller eddy length scale definition in the `CHAN2.ILES.1.15` resulted in an extended and increased drop of skin friction, indicating a increased development length, when compared to cases with higher length scales.

Near the end of the mesh, a slight drop of C_{f_b} can be observed, coinciding with the last 3 grid cells. Considering the stencil width of the 5th order WENO scheme, this effect can be attributed to a standard non-reflective boundary condition implemented in this version of Eagle3D, i.e., constant velocity downstream of the outflow and prescribed back pressure.
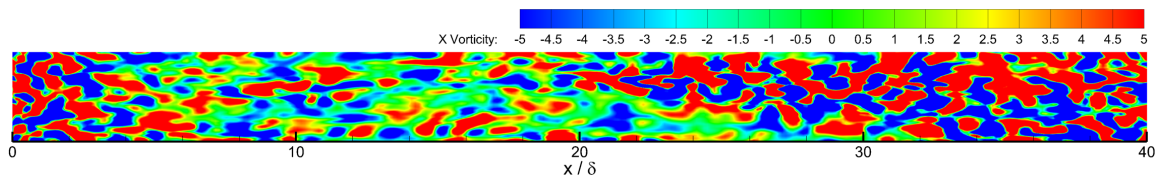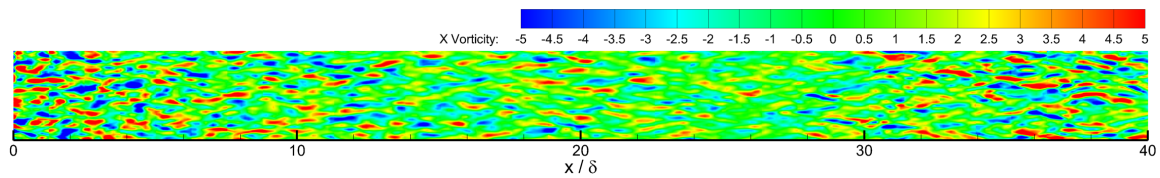

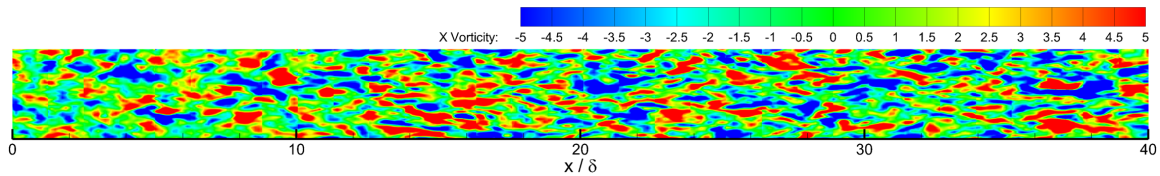(a) `CHAN2.ILES.1.15` case
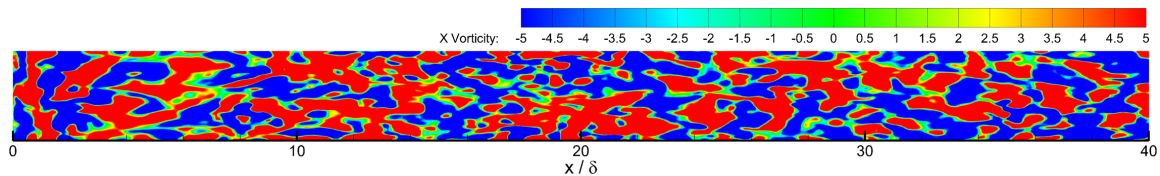
(b) `CHAN2.ILES.1.40` case

Figure 4.9 Comparison of streamwise component of instantaneous vorticity in the `CHAN2.ILES.1.15/40` cases at wall parallel planes at $z/\delta = 0.05$

Fig. 4.9 illustrates the streamwise component of instantaneous vorticity at $z/\delta = 0.05$, and reaffirms the assumption that for the `CHAN2.ILES.1.15` case, the smaller turbulent structures get dissipated and subsequently recreated. For the `CHAN2.-ILES.1.40` case, the larger structures can be fully sustained by the mesh. These observations correspond to a general characteristic of a SEM in which structures close to or under the minimal size supported by the grid tend to get dissipated out.

Larger than physical structures get broken up by the Navier-Stokes equation until reaching plausible size, preserving the majority of the turbulent kinetic energy. This behavior with higher transport of energy from lower towards greater wave numbers is consistent with observations by Jarrin (Jarrin et al., 2006) and a well documented characteristic of general turbulence (Davidson, 2009; Pope, 2015). While users of a SEM should always aim towards an accurate choice of length scale, structures should always be defined above the minimum size sustainable by the mesh to avoid accidental dissipation even if this means larger than real eddy sizes (Jarrin et al., 2006).

(a) `CHAN2.ILES.1.15` case

(b) `CHAN2.ILES.1.40` case

Figure 4.10 Comparison of streamwise component of instantaneous vorticity in the `CHAN2.ILES.1.15/40` cases at wall parallel planes at $z/\delta = 1$

Fig. 4.10 plotting the streamwise component of instantaneous vorticity at $z/\delta = 1$ (centerline plane) gives similar behavior. Turbulent structures are noticeable smaller in the `CHAN2.ILES.1.15` case and largely dissipated by the time the flow reaches the $x = 20\,\delta$. The increased turbulence downstream is generated by the the LES

itself, thereby resembling a result from an incomplete recycling method, with the SEM providing an initial disturbance. The larger structures of the `CHAN2.ILES.1.40` case are fully sustained and result is a shorter development length. The prominent decrease of eddy size between the inlet and $x \approx 15\,\delta$ indicates that the $40\%\,\delta$ initial turbulent length scale is too large and the Navier-Stokes equations break up these large structures and results in more physically sustainable values.
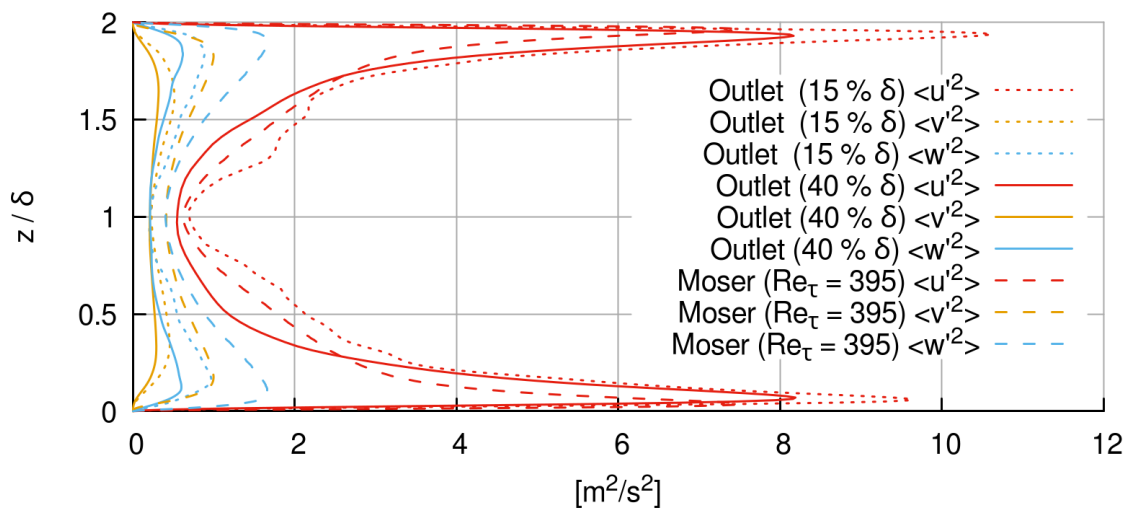

Figure 4.11 Comparison of Reynolds normal stresses in the `CHAN2.ILES.1.15/40` cases with DNS results by Moser (Moser et al., 1999)

Comparison of the Reynolds normal stresses in fig. 4.11 for the `CHAN2.ILES.1.15` case with DNS data shows a overrepresentation of streamwise turbulence components while underpredicting spanwise and wall-normal components. However, spatial resolution of the `CHAN2.ILES.1.15` case is substantially improved by the higher resolution grid. The `CHAN2.ILES.1.40` case reduces the overprediction of streamwise
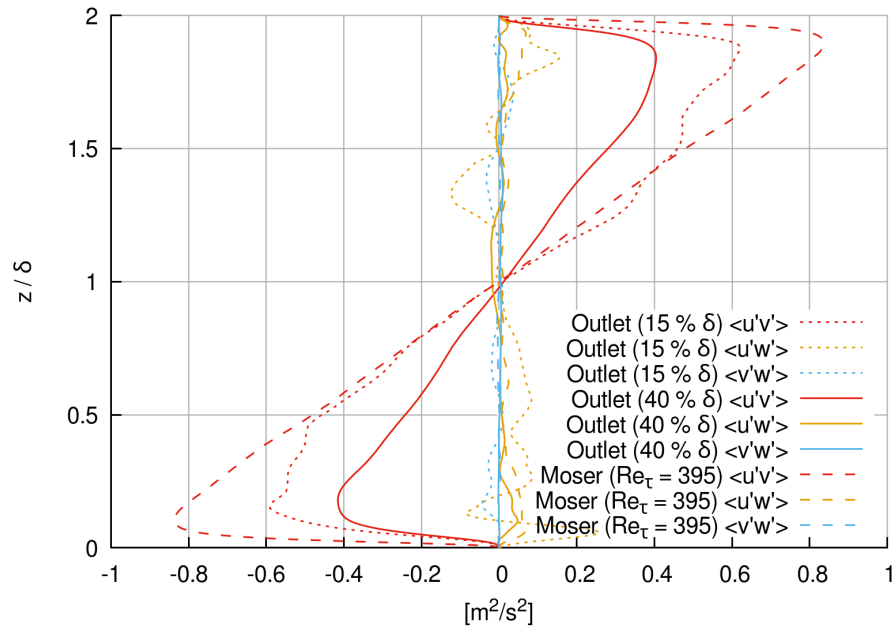
Figure 4.12 Comparison of Reynolds shear stresses in the `CHAN2.ILES.1.15/40` cases with DNS results by Moser (Moser et al., 1999)

turbulence but also decreases the already underrepresented other two components of the Reynolds normal stresses. All $15\%\,\delta$ cases show a distinctive "nose" in the streamwise component of the Reynolds normal stresses, manifesting in a drop of $\langle u'^2 \rangle$ when exceeding $50\%\,\delta$ but fully recovering on the centerline, with the cause remaining unknown.

Plots of Reynolds shear stresses in fig. 4.12 indicate improved performance for the $15\%\,\delta$ eddy size case. While both cases, $15\%\,\delta$ and $40\%\,\delta$, underestimate the overall amount of stream-spanwise vorticity, the $15\%\,\delta$ case gives the correct centerline $\langle u'v' \rangle$ gradient and higher total values, as expected from the previously shown higher $\langle u'^2 \rangle$

results. All data appears reasonably accurate for a comparison of LES results with DNS data.
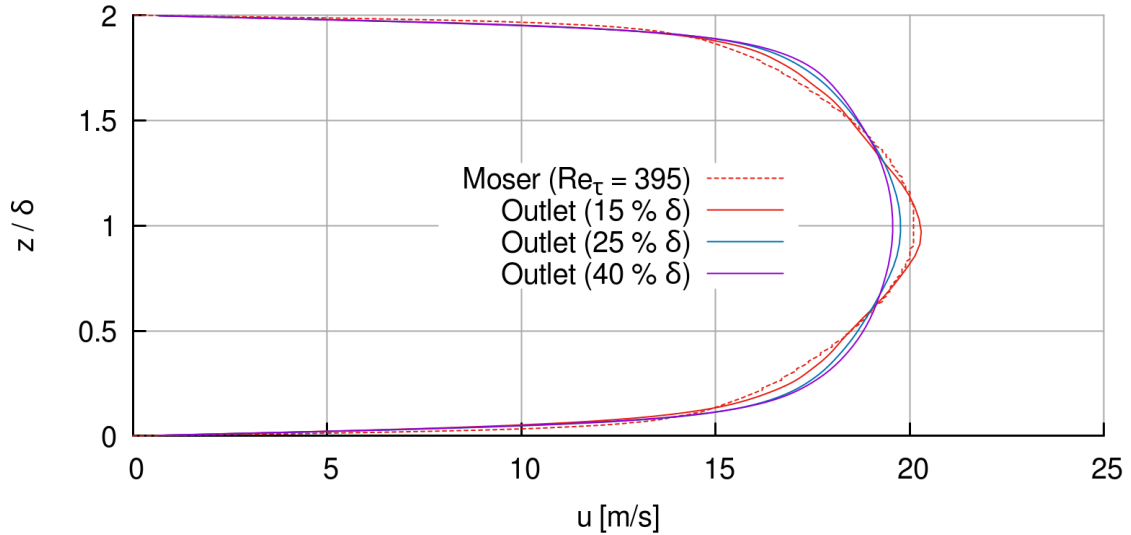

Figure 4.13 Comparison of axial velocity in the `CHAN2.ILES.1.15-40` cases with DNS results by Moser (Moser et al., 1999)

Profiles for axial velocity in fig. 4.13 are too "full" when compared to DNS data despite a lower wall gradient. The best approximation is given by the $15\%\,\delta$ case, again showing a drop in magnitude near the channel quarterlines. Calculated friction Reynolds number Re_τ at the outflow varies only slightly, ranging from 301.42 for the `CHAN2.ILES.1.15` case to 304.76 for the `CHAN2.ILES.1.40` case. This is a substantial improvement compared to the `CHAN1` case but well below the upstream $Re_\tau = 395$ from DNS (Moser et al., 1999).

4.2.5 Influence of Multiple SEM Layers

Plots for C_{f_b}, axial velocity and Reynolds normal stresses for the multi-layer SEM (i.e., `CHAN2.ILES.3.25`) case compared to the single-layer SEM (i.e., `CHAN2.ILES.1.-25`) case are given in fig. 4.14 and fig. 4.15, respectively.
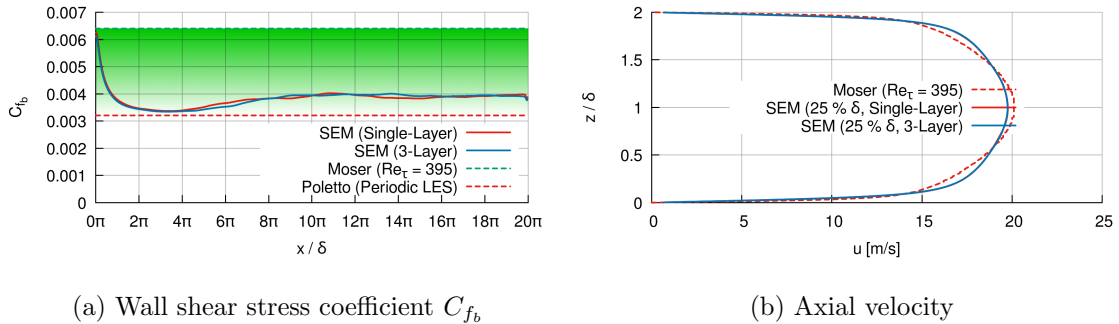

(a) Wall shear stress coefficient C_{f_b}

(b) Axial velocity

Figure 4.14 Comparison of wall shear stress coefficent C_{f_b} and axial velocity in the `CHAN4.ILES.1.25` case and `CHAN4.ILES.3.25` case with DNS results by Moser (Moser et al., 1999) and LES results by Poletto (Poletto et al., 2013)

Skin friction coefficient C_{f_b} and axial velocity in fig. 4.14 are virtually indistinguishable between both cases, thereby demonstrating the reproducibility of results and precision of the performed averaging procedure, but giving no benefit to the multi-layer SEM with 3 times the computational expense.

Reynolds normal stresses in fig. 4.15 confirm the difference between single- and multi-layer SEM to be small. A slight benefit is found for the $\langle u'^2 \rangle$ component of the multi-layer SEM. Given the fact the multi-layer formulation can increase SEM run time by orders of magnitude because of the large spacing of cells in streamwise direction, the overall benefit of the multi-layer SEM remains questionable.
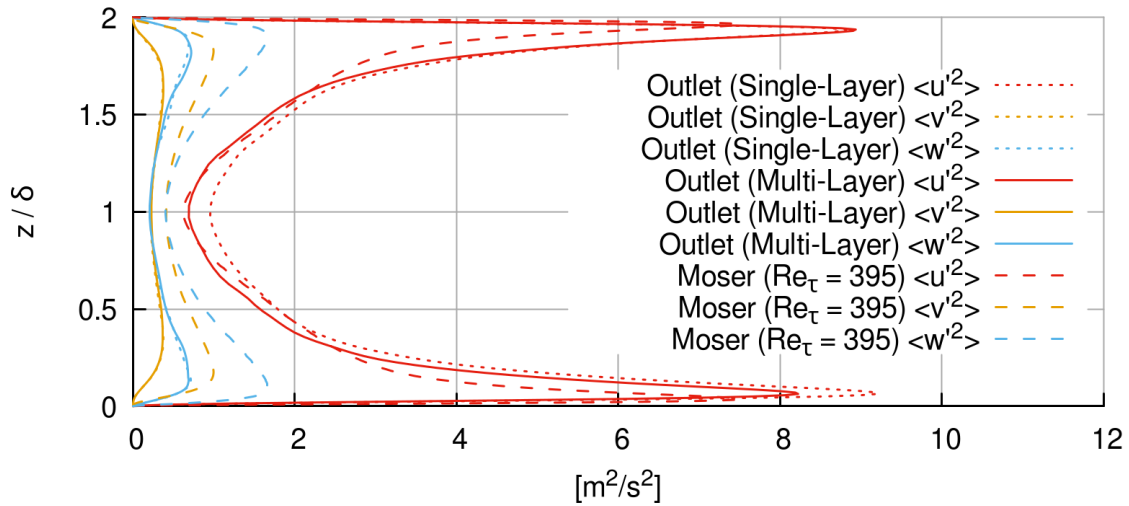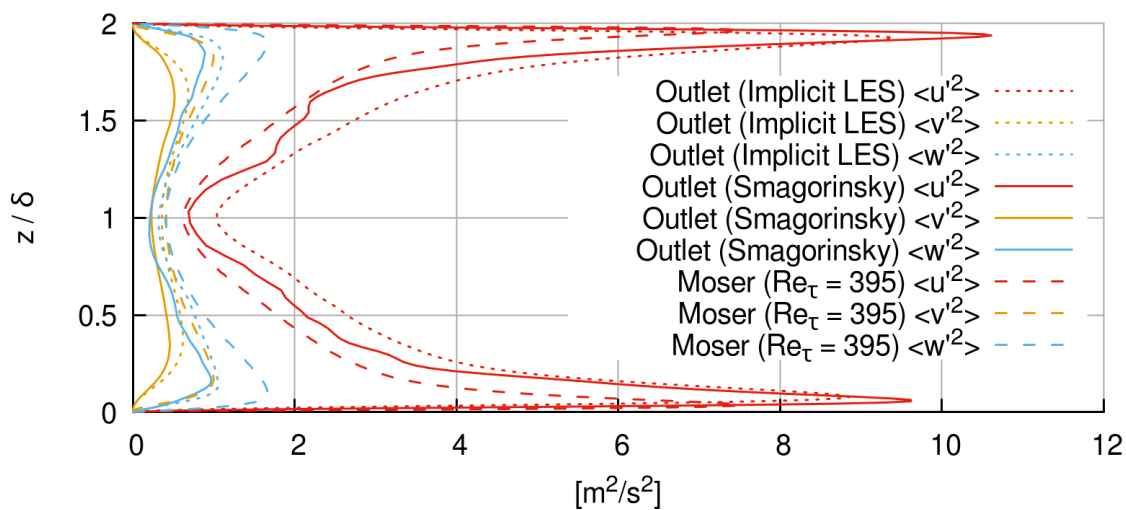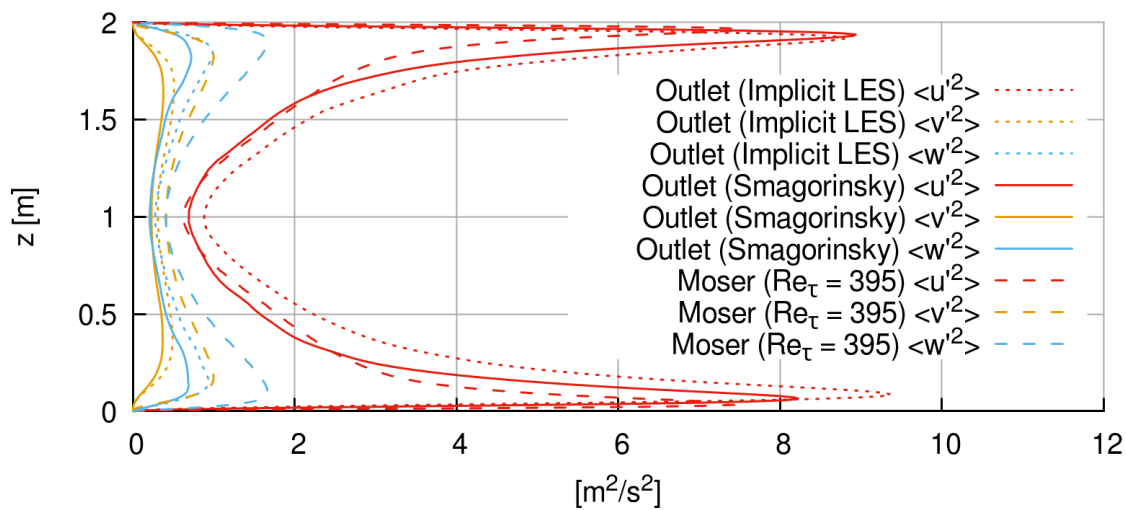
Figure 4.15 Comparison of Reynolds normal stresses in the `CHAN4.ILES.1.25` case and `CHAN4.ILES.3.25` case with DNS results by Moser (Moser et al., 1999)

4.2.6 Influence of Smagorinsky Subgrid Model

Comparisons of normal and shear components of the Reynolds stresses are given in fig. 4.16 and fig. 4.17, respectively, to illustrate the effect of a subgrid model. The Smagorinsky subgrid model improved the reproduction of turbulent stresses near the middle of the channel, most notably for by lowering the streamwise component of the normal stresses. Asymmetrical data in fig. 4.16a can most likely be attributed to an insufficient averaging length of the unsteady data. A negative effect of the increased dissipation through the Smagorinsky model is increased dampening of the already underpredicted spanwise and wall-normal components of the Reynolds normal stresses throughout the channel.

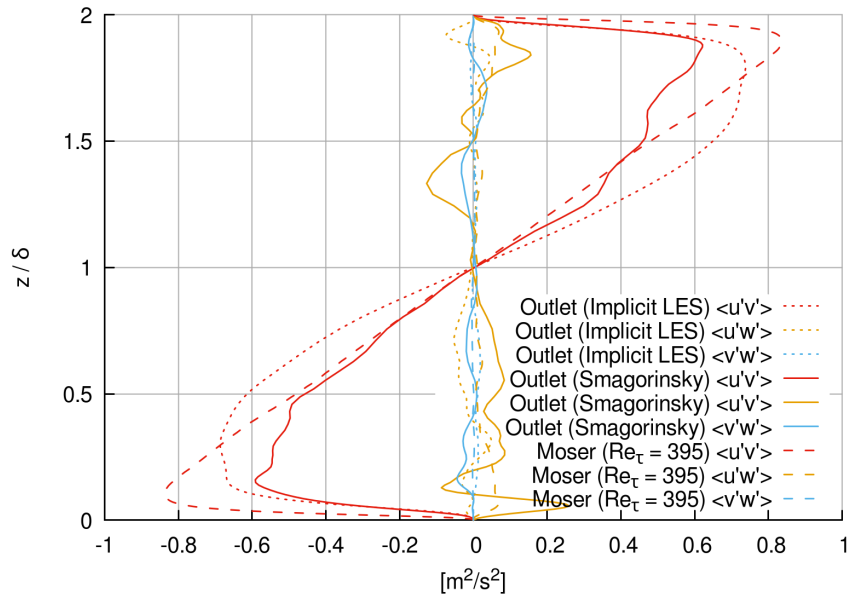(a) `CHAN2.ILES/SMAG.3.15` case

(b) `CHAN2.ILES/SMAG.3.25` case

Figure 4.16 Comparison of Reynolds normal stresses in the `CHAN2.ILES/SMAG.3.15/25` cases with DNS results by Moser (Moser et al., 1999)

(a) `CHAN2.ILES/SMAG.3.15` case
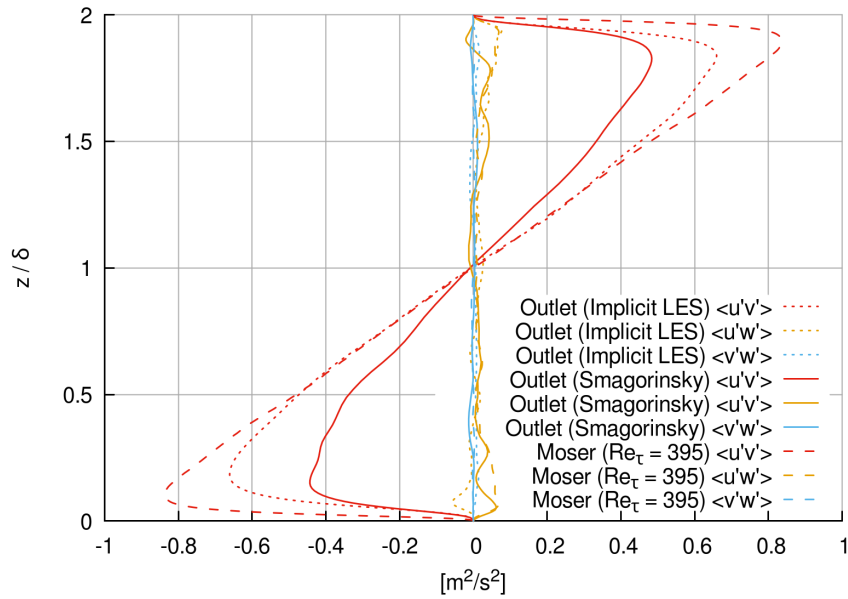

(b) `CHAN2.ILES/SMAG.3.25` case

Figure 4.17 Comparison of Reynolds shear stresses in the `CHAN2.ILES/SMAG.3.15/25` cases with DNS results by Moser (Moser et al., 1999)

Reynolds shear stresses show no large benefit for either explicit or implicit LES. The SGS model overall reduces the shear stress gradient of the $\langle u'v' \rangle$ component near the wall. This sensitivity benefits the `CHAN2.ILES/SMAG.3.15` case where this gradient was overpredicted by ILES, but impairs the `CHAN2.ILES/SMAG.3.25` case which already had the correct gradient. Shear stresses in near-wall regions are generally reduced through the added viscosity of the Smagorinsky model, thereby reducing the accuracy of the results in these areas.
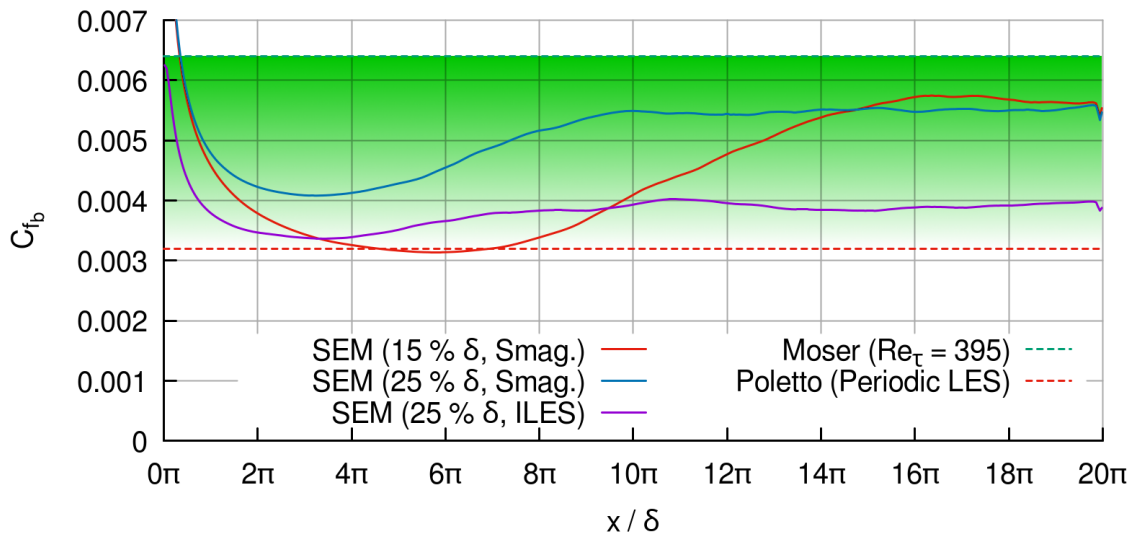
Figure 4.18 Comparison of wall shear stress coefficient C_{f_b} in the `CHAN2.ILES.3.15/25` cases with DNS results by Moser (Moser et al., 1999) and LES results by Poletto (Poletto et al., 2013)

Wall shear stress coefficient C_{f_b} plotted in fig. 4.18 shows substantial improvement using the Smagorinsky subgrid model, regardless of the chosen eddy length scale. Average C_{f_b} at the outlet is predicted as 13% lower than DNS data by Moser (Moser et al., 1999) with the Smagorinsky model, as opposed to 38% lower with implicit

LES. The reader should be aware that effective viscosity differs between implicit and explicit LES cases according to eqn. (2.15) which accounts for much of this improvement. Development length for both cases increased because of the additional dissipation introduced through the SGS model. The $15\%\,\delta$ case produces the longest development length, similar to the results with implicit LES.

4.3   Flow over a Flat Plate

4.3.1   Convergence

All simulations were performed in the Eagle3D CFD solver with the SEM running separately as a precursor simulation. Residual curves for all fully turbulent channel flow simulations show satisfactory behavior with an exemplary plot given in fig. 4.19. Residuals are normalized against the value of the first iteration which corresponds to the RANS initialization. Therefore, residuals can converge at values higher than unity once the simulation becomes fully unsteady LES. The higher residuals for the continuity equation, relative to fig. 4.3, may be related to the SEM being applied to the approximate boundary layer height , but abruptly omitted above.
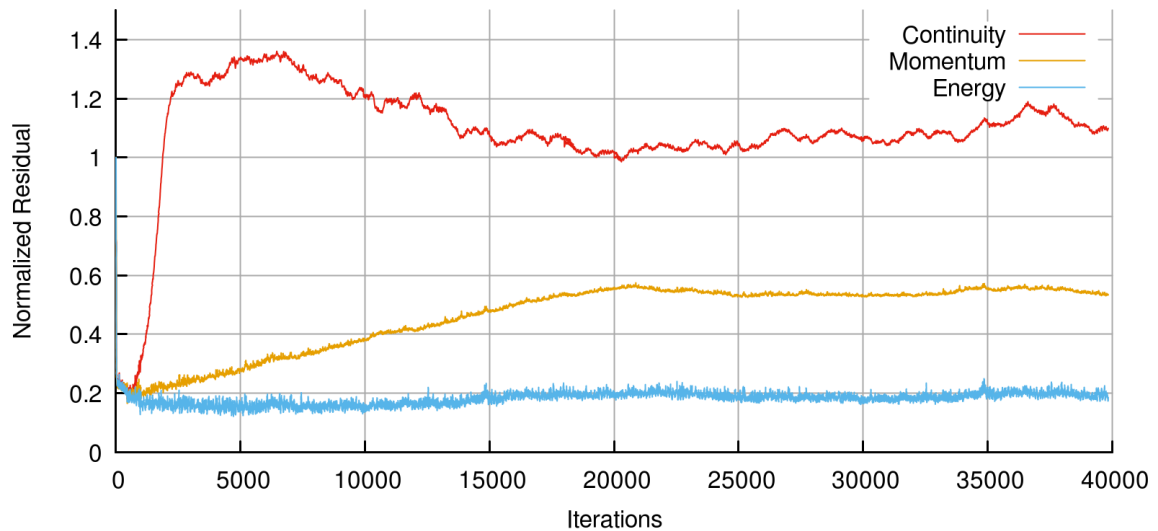

Figure 4.19 Residual curves for the flow over a flat plate

4.3.2 Influence of the Upstream RANS Model

Comparisons of axial velocity and Q criterion for the flat plate test with isotropic Shear-Stress-Transport (SST) and anisotropic Wilcox-Stress-Baseline (BSL) upstream model are given in fig. 4.20 and fig. 4.21, respectively. It was speculated that anisotropic Reynolds stresses at the SEM-generated inflow plane may results in a shorter development length.
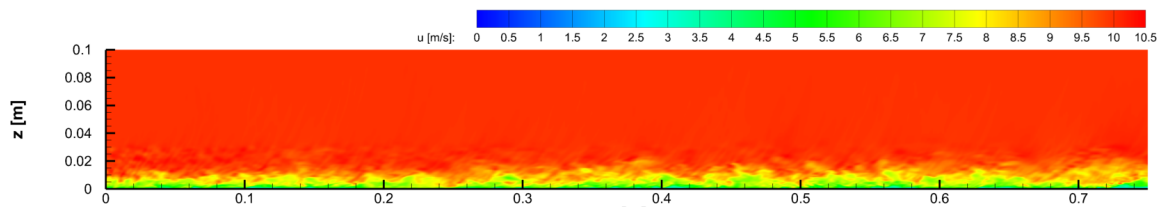
(a) Shear-Stress Transport (SST) Model
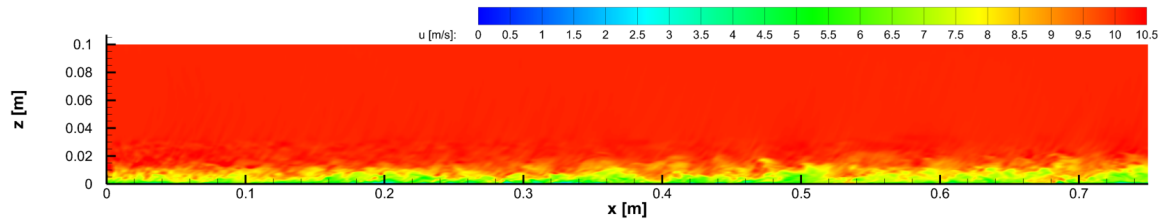
(b) Wilcox-Stress-Baseline (BSL) Model

Figure 4.20 Comparison of axial velocity of the SST and RSM upstream profiles for the flat plate case

Axial velocity contours for both simulations show turbulent behavior is sustained throughout the domain with no noticeable breakdown after the inlet. Boundary layer growth rate is visually comparable to the analytic solution by Schlichting (Schlichting, 2017) as

$$\delta \approx \frac{0.37x}{Re_x^{0.2}} \tag{4.2}$$

when accounting for the sampling position of the upstream RANS simulations at $x = 0.8\,m$. Turbulence is limited to the boundary layer with no unexpected free-stream disturbances. Despite the SST model producing an isotropic upstream solution, the results are qualitative comparable to the anisotropic BSL model once the full Navier-Stokes equations are applied.

(a) Shear-Stress Transport (SST) Model

(b) Wilcox-Stress-Baseline (BSL) Model
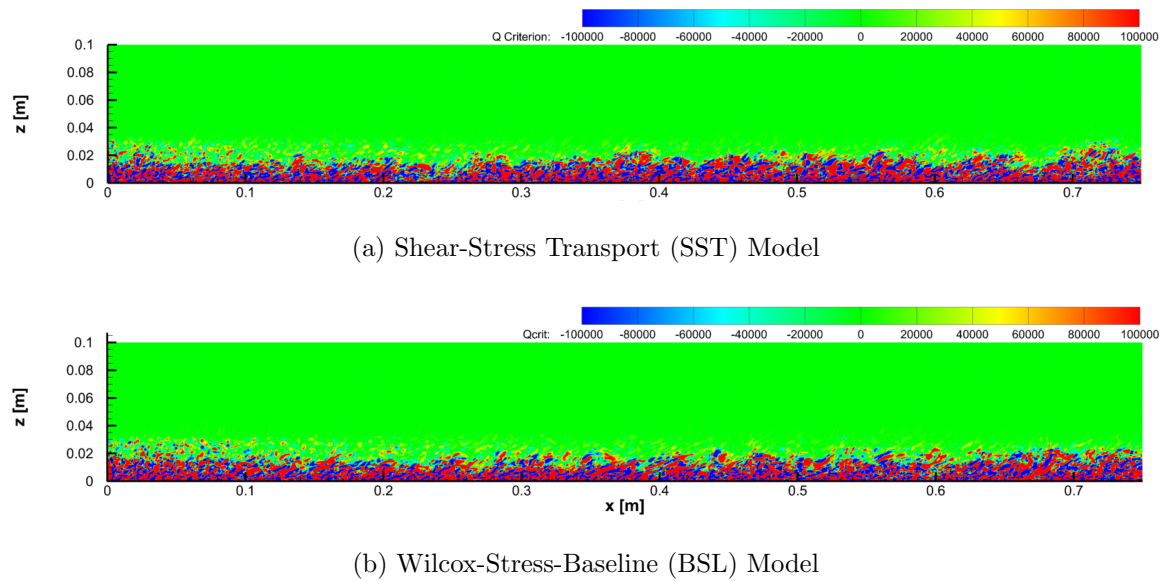
Figure 4.21 Comparison of Q criterion for the SST and RSM upstream profiles for the flat plate case

Plots of Q criterion in fig. 4.21 show comparable patterns for both RANS models. Turbulence in the boundary layer is stable on the entire plate. As the SEM creates virtual eddies randomly on the inlet plane, a small percentage of eddies with high wall-normal distance are noticeable in both cases which get dissipated by the full Navier-Stokes equations within the first $0.25\,m$ ($\approx 9.5\,\delta$).
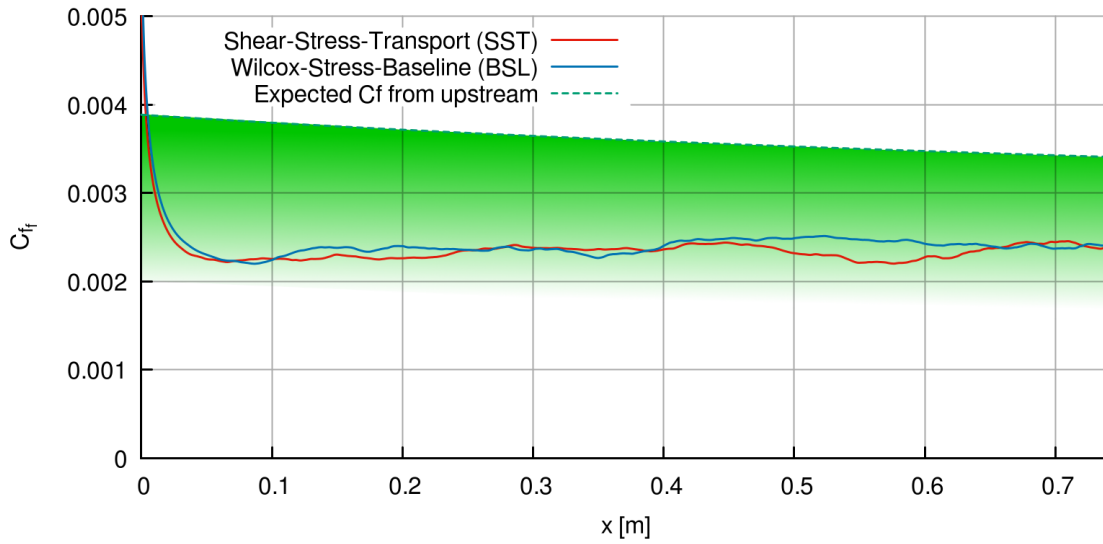
Figure 4.22 Comparison of wall shear stress coefficent C_{f_f} for the SST and BSL upstream profiles for the flat plate case with expected C_{f_f} from DNS results by Schlatter et al. (Schlatter & Örlü, 2010)

Wall shear stress coefficients for both cases are plotted in fig. 4.22. According to Schlichting (Schlichting, 2017), skin friction coefficient is expected as

$$C_{f_f} = \frac{0.0594}{Re_x^{0.2}} \tag{4.3}$$

Skin friction coefficient at the inlet has been determined by Schlatter et al. as $C_{f_f} = 0.003885$ for $Re_\theta = 1410$ (Schlatter & Örlü, 2010) and is expected to decrease proportional to $1/x^{0.2}$, according to Schlichting, as the boundary layer grows. SEM results show sharp decline of wall shear stress immediately after the inlet when Navier-Stokes equations are applied. Stable magnitudes are achieved after approximately $0.15\,m$ or $\approx 6\,\delta$ with BSL case results overall slightly higher but within the margin of sampling error. Skin friction of both SEM cases is constant after the de-

velopment length with C_{f_f} error, compared to Schlatter, decreasing with the growing boundary layer thickness.
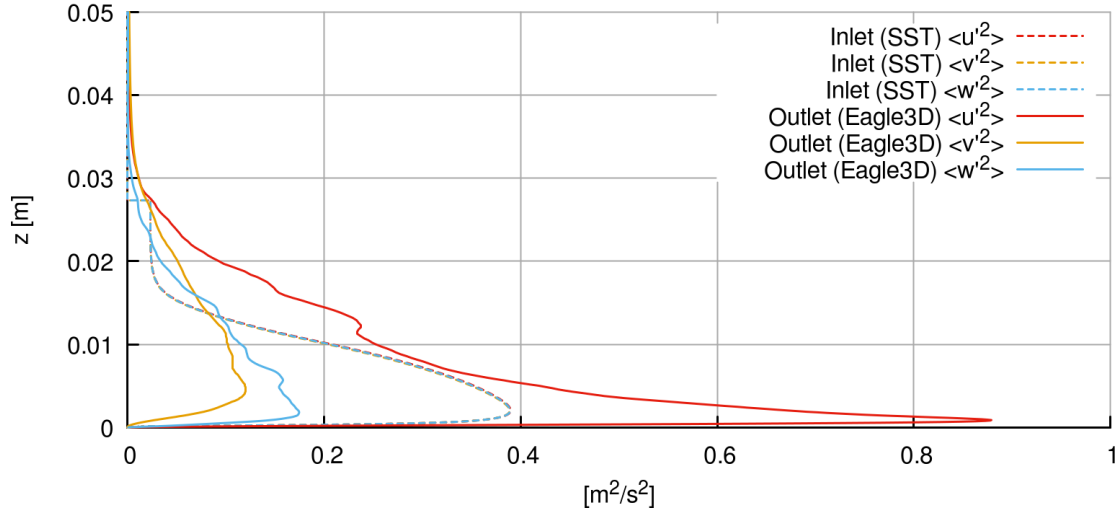
(a) Shear-Stress Transport (SST) Model
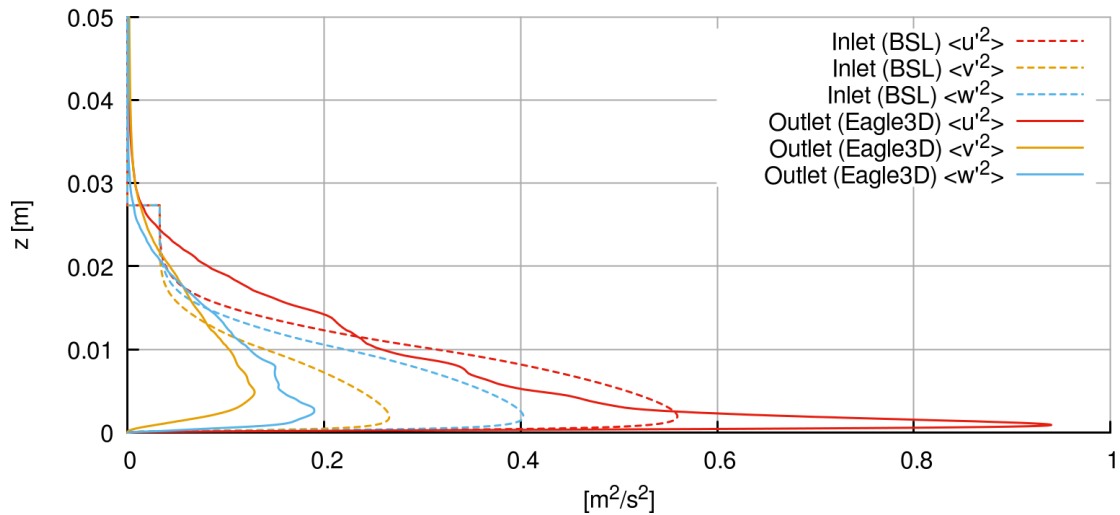
(b) Wilcox-Stress-Baseline (BSL) Model

Figure 4.23 Comparison of Reynolds normal stresses for the SST and BSL upstream profiles with their respective outlet data

Plots of generated Reynolds normal stresses at the outlet compared with their respective RANS profiles are provided in fig. 4.23 show comparable results between both cases. The sharp drop to zero at $z = 0.02735\,m$ in both cases marks the end of the SEM inflow domain. The application of the unrealistic isotropic SST solution at the inflow plane results in more turbulent fluctuations in the streamwise direction compared to the BSL case but is within the margin of sampling error for the unsteady LES simulation. Both simulations reproduce the correct order of magnitude with $\langle u'^2 \rangle > \langle v'^2 \rangle > \langle w'^2 \rangle$ independent of the upstream solution, emphasizing the robustness of the combination of SEM and Eagle3D to converge on plausible results.
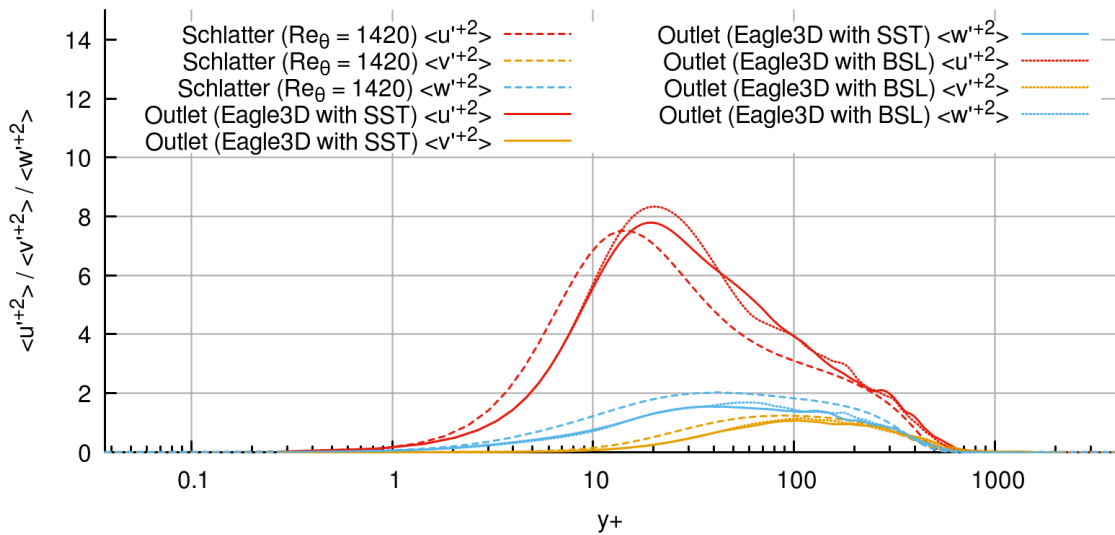
Figure 4.24 Comparison of Reynolds normal stresses for the SST and BSL upstream profiles for the flat plate case with DNS results by Schlatter et al. (Schlatter & Örlü, 2010)

Reynolds normal stresses normalized by their respective friction velocity are plotted in fig. 4.24 and compared with DNS data for $Re_\theta = 1410$ from Schlatter et

al. (Schlatter & Örlü, 2010). Both simulations show overall good agreement. The most prominent differences are a shift to higher wall-normal distances of the Eagle3D results and higher streamwise Reynolds normal stresses at the expense of weaker spanwise and wall-normal components. Overprediction of $\langle u'^{+2} \rangle$ in Eagle3D results, relative to Schlatter et al., is approximately $18\,\%$, and remarkable for a comparison of LES results with DNS data.

5. Conclusion and Future Work

The Eagle3D flow solver with a novel Bounded Central Differencing (BCD) flux scheme was combined with a Synthetic Eddy Method (SEM). Numerical simulations were performed to verify the reproduction of an unsteady turbulent flow field and evaluate the performance of a SEM combined with a density-based solver.

Comparison of the results for the flow over a cylinder simulated by Eagle3D with data from ANSYS Fluent confirms the ability of Eagle3D to accurately resolve unsteady turbulent eddy fields. Overall flow patterns and magnitudes match between both solvers with Eagle3D's high-order schemes resulting in higher fidelity.

The SEM was shown to have the ability to reproduce an unsteady turbulent velocity field from an arbitrary Reynolds stress distribution given by RANS or averaged DNS data. It has been demonstrated that the SEM provides a fast (in the meaning of low computational effort) and reliable way to start turbulent behavior for the flow in a channel or on a flat plate. Accuracy of the SEM was estimated using components of the velocity vector, skin friction coefficient and Reynolds stresses. It has been concluded that LES results of Eagle3D combined with an SEM show qualitative correct result in all metrics given sufficient grid resolution but are quantitatively unable to reach DNS-like quality.

Parametric studies were performed on the influence of grid resolution, eddy length scale, ghost cell treatment and SGS model on LES results. The moderate mesh refinement from 1.886 million to 5 million cells resulted in substantial benefits for the turbulent channel case. The SEM development length was significantly reduced and flow statistics were more accurate than the periodic LES performed by Poletto et al. on the coarse grid (Poletto et al., 2013).

The eddy length scale was shown to directly influence the development length. A minimum length scale is required to sustain the coherent SEM perturbations and avoid breakdown into a random function. Higher values resulted in shorter development lengths. However, as eddy length scale increases, there is diminishing improvement since the turbulent structures are already fully sustainable by the mesh. Turbulent statistics taken after the development length were demonstrated to converge on similar results.

It was speculated that a multi-layer SEM providing accurate reconstructions for all ghost cells used by the high-order WENO scheme would result in better reproduction of spanwise and wall-normal turbulent statistics than the classical single-layer formulation. This assumption could not be proven, with no clear benefit for any version evident.

Implementation of the Smagorinsky subgrid model resulted in an overall reduction of turbulent statistics. This benefited cases with short prescribed eddy length scale where values were overpredicted by ILES, but impaired results of cases with higher eddy length scales where the Reynolds stresses were already correct or too

low. Statistics of the wall shear stress coefficient showed substantial improvement using the SGS model, with the error compared to DNS data by Moser et al. reduced by more than 50% (Moser et al., 1999). Much of this improvement is attributed to the higher effective viscosity of the SGS model case.

Recommended Future Work   Further studies are required on the influence of the utilized eddy shape function on LES results. Both Jarrin et al. and Poletto et al. attempted various definitions (Jarrin et al., 2006, 2009; Poletto et al., 2011, 2013) but no data has been published on performance using a density-based code.

The unique formulation of a Jarrin style SEM, relating a isotropic random function to anisotropic Reynolds stresses, allows for adjustments to the Lund coefficients to enhance underestimated Reynolds stress components. Additional research is necessary to ascertain if constant multiplication factors for these coefficients can be found and how modifications influence other flow parameters.

Fluctuations in the energy field have been demonstrated to be negligible for the low-speed cases covered in this thesis. Moving to trans- and supersonic flow regimes as covered in proposed areas of application of the Eagle3D flow solver, thermal stresses will require consideration to ensure correct representation of the complete turbulent energy. Formulations to account for energy fluctuations might have to go beyond the assumption of isotropic flow formulation depending on the given upstream data.

REFERENCES

Alfonsi, G., Ciliberti, S., Mancini, M., & Primavera, L. (2016, February). Direct numerical simulation of turbulent channel flow on high-performance GPU computing system. *Computation*, *4*(1), 13. doi: 10.3390/computation4010013

Anderson, J. D. (1995). *Computational fluid dynamics* (International ed.). New York, USA: McGraw-Hill.

ANSYS, Inc. (2010, December). Introduction to ANSYS Fluent (13.0 ed.) [Computer software manual]. 2600 Ansys Dr, Canonsburg, USA.

Blevins, R. D. (1990). *Flow-induced vibration* (Second edition, Ed.). Van Nostrand Reinhold.

Davidson, P. A. (2009). *Turbulence* (Reprinted ed.). Oxford [u.a.]: Oxford Univ. Press.

Dean, R. B. (1978). Reynolds number dependence of skin friction and other bulk flow variables in two-dimensional rectangular duct flow. *Journal of Fluids Engineering*, *100*(2), 215. doi: 10.1115/1.3448633

Druault, P., Largeau, J. F., Coiffet, F., Delville, J., Bonnet, J. P., & Lardeau, S. (2005). Numerical investigations of turbulent inflow condition generation for LES. *Journal of Fluids Engineering*, *127*(5), 945. doi: 10.1115/1.2012499

Engblom, W. A., Fletcher, B., & Georgiadis, N. J. (2007). Validation of conjugate heat-transfer capability for water-cooled high-speed flows. In *Proceedings of the 39th American Institute of Aeronautics Astronautics Thermophysics Conference, Miami, Fl, USA* (pp. 25–28).

Ferziger, J. H. (2008). *Numerische Strömungsmechanik* (M. Perić, Ed.). Berlin, Germany: Springer.

Francois, D. G. (2015, April). *Numerical simulation of engine-inlet stall at low speed range with reynolds-stress turbulence models.* Gauss Centre for Supercomputing. Retrieved from `http://www.gauss-centre.eu/gauss-centre/EN/Projects/CSE/2015/Francois_NSESRSM.html?nn=1345710` (Online; accessed 25-September-2017)

Geurts, K. J., Meinke, M., & Schröder, W. (2013). A zonal RANS/LES method for the flow around an airfoil at high angle of attack. In *Notes on numerical fluid mechanics and multidisciplinary design* (pp. 465–472). Springer Berlin Heidelberg.

Hunt, J. C., Wray, A. A., & Moin, P. (1988, December). Eddies, streams, and convergence zones in turbulent flows. In *Studying Turbulence Using Numerical Simulation Databases, 2. Proceedings of the 1988 Summer Program.* Stanford University; CA, United States.

Jarrin, N. (2008). *Synthetic inflow boundary conditions for the numerical simulation of turbulence* (Unpublished doctoral dissertation). School of Mechanical, Aerospace and Civil Engineering, The University of Manchester, Manchester M60 1QD, United Kingdom.

Jarrin, N., Benhamadouche, S., Laurence, D., & Prosser, R. (2006). A synthetic-eddy-method for generating inflow conditions for large-eddy simulations. *International Journal of Heat and Fluid Flow*, *27*(4), 585–593.

Jarrin, N., Prosser, R., Uribe, J.-C., Benhamadouche, S., & Laurence, D. (2009). Reconstruction of turbulent fluctuations for hybrid rans/les simulations using a synthetic-eddy method. *International Journal of Heat and Fluid Flow*, *30*(3), 435–442.

Jiang, G.-S., & Shu, C.-W. (1996, June). Efficient implementation of weighted ENO schemes. *Journal of Computational Physics*, *126*(1), 202–228. doi: 10.1006/jcph.1996.0130

Klein, M., Sadiki, A., & Janicka, J. (2003, April). A digital filter based generation of inflow data for spatially developing direct numerical or large eddy simulations. *Journal of Computational Physics*, *186*(2), 652–665. doi: 10.1016/s0021-9991(03)00090-1

Lamanna, G., Spring, S., Schindler, A., & Sotgiu, C. (2015). *Fundamentals of turbulence modelling.* University of Stuttgart. (Unpublished lecture notes)

Lee, S., Lele, S. K., & Moin, P. (1992, July). Simulation of spatially evolving turbulence and the applicability of taylor's hypothesis in compressible flow. *Physics of Fluids A: Fluid Dynamics*, *4*(7), 1521–1530. doi: 10.1063/1.858425

Lilly, D. K. (1967). The representation of small-scale turbulence in numerical simulation experiments. In *IBM Scientific Computing Symposium on Environmental Sciences*.

Lund, T. S., Wu, X., & Squires, K. D. (1998, March). Generation of turbulent inflow data for spatially-developing boundary layer simulations. *Journal of Computational Physics*, *140*(2), 233–258. doi: 10.1006/jcph.1998.5882

Meneveau, C. (2010). Turbulence: Subgrid-scale modeling. *Scholarpedia*, *5*(1), 9489. doi: 10.4249/scholarpedia.9489

Moser, R. D., Kim, J., & Mansour, N. N. (1999). Direct numerical simulation of turbulent channel flow up to $Re_\tau = 590$. *Physics of Fluids*, *11*(4), 943–945.

OpenCFD Ltd. (2016, June). *OpenFOAM® v1606+: New Boundary Conditions - Inflow turbulence generator.* Retrieved from http://www.openfoam.com/releases/openfoam-v1606+/boundary-conditions.php (Online; accessed 5-October-2017)

Poletto, R., Craft, T., & Revell, A. (2013). A new divergence free synthetic eddy method for the reproduction of inlet flow conditions for les. *Flow, turbulence and combustion*, *91*(3), 519–539.

Poletto, R., Revell, A., & Craft, T. (2012). A new divergence-free synthetic eddy method for full reproduction of inlet flow conditions for embedded les. In *Proceedings of 9th International ERCOFTAC Symposium on Engineering Turbulence Modelling and Measurements, Tessaloniki, Greece*.

Poletto, R., Revell, A., Craft, T. J., & Jarrin, N. (2011). Divergence free synthetic eddy method for embedded les inflow boundary conditions. In *Seventh international symposium on turbulence and shear flow phenomena (TSFP-7), Ottawa.*

Pope, S. B. (2015). *Turbulent flows* (12. print. ed.). Cambridge [u.a.]: Cambridge Univ. Press.

Roller, S., & Munz, C.-D. (2000, May). A low mach number scheme based on multi-scale asymptotics. *Computing and Visualization in Science*, *3*(1-2), 85-91. doi: 10.1007/s007910050055

Rynell, A., Efraimsson, G., Chevalier, M., & Abom, M. (2016, jun). Inclusion of upstream turbulent inflow statistics to numerically acquire proper fan noise characteristics. In *SAE technical paper series.* SAE International. doi: 10.4271/2016-01-1811

Sagaut, P., Deck, S., & Terracol, M. (2013). *Multiscale and multiresolution approaches in turbulence* (2. ed. ed.). London: Imperial College Pr.

Schiavo, L. A. C., de Jesus, A. B., Wolf, W. R., & Azevedo, J. L. F. (2013, November). A study of turbulent flows in 2-d channels using large eddy simulations. In *22nd international congress of mechanical engineering (COBEM 2013).* Ribeirão Preto, SP, Brazil.

Schlatter, P., & Örlü, R. (2010, July). Assessment of direct numerical simulation data of turbulent boundary layers. *Journal of Fluid Mechanics*, *659*, 116–126. doi: 10.1017/s0022112010003113

Schlatter, P., & Örlü, R. (2011, December). Turbulent asymptotic suction boundary layers studied by simulation. *Journal of Physics: Conference Series*, *318*(2), 022020. doi: 10.1088/1742-6596/318/2/022020

Schlichting, H. (2017). *Boundary-layer theory* (Ninth edition ed.; K. Gersten, E. Krause, H. Oertel, & K. Mayes, Eds.). Berlin: Springer.

Smagorinsky, J. (1963, March). General circulation experiments with the primitive equations. *Monthly Weather Review*, *91*(3), 99–164. doi: 10.1175/1520-0493(1963)091¡0099:gcewtp¿2.3.co;2

Tajallipour, N., Owlam, B. B., & Paraschivoiu, M. (2009, May). Self-adaptive upwinding for large eddy simulation of turbulent flows on unstructured elements. *Journal of Aircraft*, *46*(3), 915–926. doi: 10.2514/1.38945

Toro, E. F., Spruce, M., & Speares, W. (1994). Restoration of the contact surface in the hll-riemann solver. *Shock waves*, *4*(1), 25–34.

Winkler, C. M., Dorgan, A., & Mani, M. (2012). A reduced dissipation approach for unsteady flows on unstructured grids. *AIAA Paper*, *570*, 2012.

Wu, X. (2017, January). Inflow turbulence generation methods. *Annual Review of Fluid Mechanics*, *49*(1), 23–49. doi: 10.1146/annurev-fluid-010816-060322

Zhang, Q., Schröder, W., & Meinke, M. (2010, August). A zonal RANS-LES method to determine the flow over a high-lift configuration. *Computers & Fluids*, *39*(7), 1241–1253. doi: 10.1016/j.compfluid.2010.02.006